Soil Permittivity Estimation Over Croplands Using Full and Compact Polarimetric SAR Data

Narayanarao Bhogapurapu (iD), *Graduate Student Member, IEEE,* Subhadip Dey (iD), *Graduate Student Member, IEEE,* Avik Bhattacharya (iD), *Senior Member, IEEE,* Carlos López-Martínez (iD), *Senior Member, IEEE,* Irena Hajnsek (iD), *Fellow, IEEE,* and Y. S. Rao (iD), *Member, IEEE*

Abstract—Soil permittivity estimation using Polarimetric Synthetic Aperture Radar (PolSAR) data has been an extensively researched area. Nonetheless, it provides ample scope for further improvements. The vegetation cover over the soil surface leads to a complex interaction of the incident polarized wave with the canopy and subsequently with the underlying soil surface. This paper introduces a novel methodology to estimate soil permittivity over croplands with vegetation cover using the full and compact polarimetric modes. The proposed method utilizes the full and compact polarimetric scattering-type parameters, θ_{FP} and θ_{CP}, respectively. These scattering type parameters are a function of the soil permittivity and the Barakat degree of polarization. The method considers the X-Bragg scattering model for the soil surface. In particular, these scattering-type parameters explicitly account for the depolarizing structure of the scattered wave while characterizing targets. Thus, the depolarization information in terms of surface roughness in the X-Bragg model gets inherent importance while using θ_{FP} and θ_{CP}, unlike existing scattering-type parameters. Therefore, the proposed technique enhances the expected value of the inversion accuracies. This study validated the major phenology stages of four crops using the UAVSAR full-pol and simulated compact pol SAR data and the ground truth data collected during the SMAPVEX12 campaign over Manitoba, Canada. The proposed method estimated permittivity with an RMSE of 2.2 to 4.69 for FP and 3.28 to 5.45 for CP SAR data along with a Pearson coefficient, $r \geq 0.62$.

Index Terms—Soil permittivity, Polarimetric SAR (PolSAR), Scattering mechanisms, Target characterization parameter, X-Bragg

I. INTRODUCTION

HIGH resolution soil permittivity/moisture estimates are critical for agro-climatic modeling [1], [2] and hydrologic forecasting [3], [4]. Hence, using Polarimetric Synthetic Aperture Radar (PolSAR) data, soil permittivity estimation is an extensively researched topic with ample scope for further improvements. Besides, estimating soil permittivity over vegetated soils is challenging and often introduces estimation bias due to the complex interaction of the polarized incident wave with the canopy structure and underlying soil surface.

In this regard, several semi-empirical models are developed primarily using the backscattered or coherence information of the polarimetric SAR. Moreover, the majority of those studies were limited to sparse vegetation conditions. Of them, Oh et al., [5], and Dubois et al., [6] utilized the backscatter amplitude

N. Bhogapurapu, A. Bhattacharya, and Y. S. Rao are with the Microwave Remote Sensing Lab, Center of Studies in Resources Engineering, Indian Institute of Technology Bombay, India, e-mail: (bnarayanarao@iitb.ac.in). S. Dey is with the Department of Agricultural and Food Engineering, Indian Institute of Technology Kharagpur, India, e-mail: (sdey23@agfe.iitkgp.ac.in)

ratios, while Borgeaud et al., [7] and Mattia et al., [8] studied the effect of polarimetric coherence for the estimation of soil moisture. Notably, the polarimetric coherence-based technique achieved better estimation accuracies than the surface scattering models for sparsely vegetated land cover types. However, it is well evident from the literature that the vegetation cover for many of the crops is more than 80%. Hence, the assumption of sparse canopy structure during the inversion of soil moisture does not hold its validity. Thus, a general approach could be separating vegetation scattering contribution from the soil layer for moderate to dense vegetative areas.

One of the approaches to separate the scattering of the vegetation layer from the soil layer is to utilize the polarimetric decomposition techniques [9]. In model-based scattering power decompositions, the geometry of the vegetation structure is considered as the incoherently integrated scattering characteristics of a cloud of canonical scatterers at different orientations within a resolution cell. These assumptions about the vegetation structure help subtract its contribution from the overall scenario. Further, the remaining scattering characteristics can be considered as the contribution of the surface scattering from the soil layer and double bounce scattering from the combined soil and crop stem structures. However, the scattering phase centers for these two scattering mechanisms could overlap, making it ambiguous to separate them from a resolution cell. In this regard, Rice [10] assumed the soil surface as Bragg, and Cloude et al., [11] considered the soil surface as X-Bragg scatterer type to invert soil permittivity from the extracted surface component.

Cloude and Corr [12] demonstrated the sensitivity of the scattering-type parameter $\overline{\alpha}$ with the soil permittivity for Bragg-type surfaces. In particular, the concept of Bragg scattering relies on the scattering from successive vertically separated smooth planes with constructive interference [13]. Hence, this model does not consider surface roughness in its formulation. In this regard, Hajnsek et al., [14] proposed a suitable incoherent surface scattering model known as the extended Bragg (X-Bragg) to account for the surface roughness. Subsequently, several studies were performed utilising improved polarimetric decomposition models [15]–[17] multi-incidence angle [15], [18] and multi-angular time series polarimetric SAR data [19], [20].

Among these approaches, the multi-incidence angle approach produced an increased inversion rate and minimized topographic effects caused by local slopes. However, one observed a high variance in the estimates for different volume

scattering models and surface roughness. Accordingly, the subsequent efforts focused on modifying the vegetation models. In this context, Jagdhuber et al., [16] proposed an iterative, generalized hybrid polarimetric decomposition to model the volume component, which incorporates a physically constrained volume intensity component. This approach uses a volume particle shape factor and an orientation distribution width to generalize the volume model and improve soil moisture inversion rate.

Subsequently, Wang et al., [17] compared the soil moisture inversion results over vegetated areas using three different model-based polarimetric decomposition techniques. Their studies showed that the incidence angles significantly impact the soil moisture estimates. Hence, it was proposed to normalize the polarimetric parameters to minimize the incidence angle effect on soil moisture retrieval. With this modification, the accuracy of the estimated soil moisture was increased using the decomposition proposed by An et al., [21]. Nevertheless, the inversion rate decreases with the increase in incidence angle. In this context, [19] proposed to use multi-incidence time series data for soil moisture estimation over low and high-vegetated agricultural fields. In particular, the inversion rate from the decomposed dihedral component at higher incidence angles is significantly improved when the surface component fails to estimate.

In another research, Shi et al., [20] proposed deterministic non-linear equations as a function of soil roughness and soil-vegetation dielectric properties. In their study, a Generalized Volume Scattering Model (GVSM) is used to capture close to actual volume contribution. However, the assumptions in the proposed technique may only be valid for some crops at diverse phenological stages. From these previous studies, it is clear that the decomposition techniques and polarimetric descriptors govern the uncertainty in the estimates. On the other hand, the estimation of these uncertainties becomes more complex in the presence of surface roughness. Therefore, using polarimetric descriptors robust towards the perturbations induced by roughness could minimize this uncertainty in estimates.

Many international space agencies have recently been interested in implementing compact polarimetric imaging modes in the SAR systems, such as in-orbit ALOS-2, Radarsat Constellation Mission (RCM), SAR Observation & Communications Satellite (SAOCOM), and upcoming NASA-ISRO SAR (NISAR). It is because compact polarimetric (CP) SAR offers many advantages over full polarimetric (FP) SAR, such as wider swath coverage, a higher incident angle range, a reduced data rate, and lower system power consumption but at the expense of reduced information.

There are several CP SAR modes depending on transmit and receive polarization, such as dual-circular compact polarimetry (DCP) [22]: right circular polarization on transmit, and right and left circular polarization on receive, hybrid-pol architecture [23]: circular transmit and orthogonal linear polarizations on receive and $\pi/4$ mode [24]: the transmitted polarization is a superposition of the linear vertical polarization (V) and horizontal (H) oriented at $45°$ to the horizontal.

Initially, the soil moisture/permittivity estimations using CP SAR data adopted the surface scattering models of bare soils developed for FP SAR data [25]. Subsequently, other data-driven approaches were also utilized, such as data cube approaches [26] machine learning techniques [27]. However, most initial studies are limited to using simulated data due to the limited availability of acquired CP SAR data.

Truong et al., [25] conducted a preliminary study to approximate simulated compact polarimetric backscatter intensities ($\sigma_{RH}^{\circ}, \sigma_{RV}^{\circ}$) using linearly polarized backscatter intensities. Subsequently, they utilized the algorithm proposed by Dubois et al., [6] to estimate soil moisture from the bare soil surface. They reported a marginal improvement (standard deviation of $0.02\,\mathrm{m^3\,m^{-3}}$) in soil moisture retrieval performance for CP SAR data than linearly polarised backscatter (HH and VV). Recently, Merzouki et al., [28] utilized a similar approach of approximating CP SAR data from FP SAR data and a surface scattering model to invert soil moisture. Unlike [25], where a relative comparison of inverted parameters from FP and CP SAR was carried out, [28] has validated the approach using in-situ soil moisture data acquired over three years. They have reported a good agreement of inverted results between FP and CP SAR but with a high bias of $0.10\,\mathrm{m^3\,m^{-3}}$.

On the other hand, Ponnurangam et al., [29] utilized RISAT-1 CP SAR data to estimate soil moisture over croplands using polarimetric decomposition and surface scattering models. Notably, [29] utilized an extended Bragg model for CP SAR data under high-frequency approximation. Therefore, using the X-Bragg model showed improved results than the Integral Equation Model (IEM) for agricultural lands. However, this approach is limited to high-frequency approximation. Based on the available literature, the present research is limited to soil permittivity/moisture estimation over croplands using CP SAR polarimetric techniques.

Moreover, the recent advancements in target characterization and polarimetric decomposition techniques using FP and CP SAR data could improve soil permittivity inversions over croplands. Dey et al., [30] proposed a scattering-type parameter θ, which is derived equivalently for both FP and CP SAR data. The θ parameter is a function of the Barakat degree of polarization and the polarimetric coherency/covariance matrix elements. It was shown in [30], [31], that θ_{FP} offers better target characterization capability than $\overline{\alpha}$ for the FP mode, while θ_{CP} provides better target characterization capability than χ for CP mode. Therefore, as pointed out by many previous studies, using advanced decomposition techniques and better target characterization techniques, one could minimize the uncertainties in the soil permittivity estimation.

This work proposes a novel framework to estimate soil permittivity over croplands using FP and CP SAR data. The proposed inversion algorithm can likewise be applied to both modalities. Dey et al., [30] demonstrated superior performance of the scattering-type parameters: (θ_{FP} and θ_{CP}) for target characterization. Therefore, it is anticipated to be effective in soil permittivity inversion over vegetated soils. We critically assess this approach to estimate surface soil permittivity using the data obtained from the SMAPVEX12 test site in Canada with the crop fields containing corn, soybean, pasture, and wheat.

This work unveils the proposal of a novel methodology of soil moisture estimation over croplands for both FP and CP SAR data in Section II. Section III provides the details of SAR and ground truth datasets utilized for validating the proposed methodologies. In Section IV, we present and discuss the soil permittivity inversion results of the proposed method for various crop types. Accordingly, Sections IV-A and IV-B present and compare the results from the proposed approach with the existing techniques for FP and CP SAR data, respectively. Finally, we summarize and conclude the proposed methodologies in Section V followed by highlighting its advantages and limitations for different SAR data for various crop types.

II. METHODOLOGY

Soil moisture retrieval algorithms primarily rely on the physical interpretation of target parameters derived from polarimetric SAR data. This study aims to develop a consistent soil permittivity retrieval algorithm for FP and CP SAR data over cultivated areas. In this regard, the performance of the set of roll-invariant scattering-type parameters θ_{FP} and θ_{CP} are explored for full and compact polarimetric data, respectively.

A. Full polarimetry

For full polarimetric SAR data, one can represent the complete backscattering information from the target with a 2×2 complex scattering matrix $\mathbf{S}$. For linear horizontal (H) and linear vertical (V) polarization basis $\mathbf{S}$ is expressed as,

$$\mathbf{S} = \begin{bmatrix} S_{\text{HH}} & S_{\text{HV}} \\ S_{\text{VH}} & S_{\text{VV}} \end{bmatrix} \tag{1}$$

where S_{HH}, S_{VV} are the co-polarized complex scattering coefficients, and S_{HV}, S_{VH} are the cross-polarized complex scattering coefficients. For a monostatic antenna configuration, the reciprocity condition (i.e., $S_{\text{HV}} = S_{\text{VH}}$) makes the scattering matrix symmetric.

The space and time-varying stochastic target scattering processes can be effectively described by the second-order information from $\mathbf{S}$. One can obtain this information through the multi-looked coherency matrix $\mathbf{T}$. The 3×3 $\mathbf{T}$ is a Hermitian positive semi-definite matrix and can be obtained from the averaged outer product of the Pauli target vector $\mathbf{k}_{\text{P}} = \frac{1}{2}\text{Tr}(\mathbf{S}\Psi_P)$ with its conjugate transpose as,

$$\mathbf{T} = \mathbb{E}\left(\mathbf{k}_{\text{P}}\mathbf{k}_{\text{P}}^{\dagger}\right) = \frac{1}{N}\sum_{i=1}^{N}\mathbf{k}_{\text{P}i}\mathbf{k}_{\text{P}i}^{\dagger} \tag{2}$$

where $\mathbb{E}$ represents the expected value of the outer product, the superscript $\dagger$ denotes the conjugate transpose operator, and N is the size of the multi-look window. The Pauli target vector, $\mathbf{k}_{\text{P}}$ is expressed in terms of scattering matrix elements as,

$$\mathbf{k}_{\text{P}} = \frac{1}{\sqrt{2}}\begin{bmatrix} S_{\text{HH}} + S_{\text{VV}} & S_{\text{HH}} - S_{\text{VV}} & 2S_{\text{HV}} \end{bmatrix}^{T} \tag{3}$$

where Ψ_{P} is the set of Pauli basis matrices for the monostatic case,

$$\Psi_{\text{P}} = \left\{ \sqrt{2}\begin{bmatrix} 1 & 0 \\ 0 & 1 \end{bmatrix}, \sqrt{2}\begin{bmatrix} 1 & 0 \\ 0 & -1 \end{bmatrix}, \sqrt{2}\begin{bmatrix} 0 & 1 \\ 1 & 0 \end{bmatrix} \right\}$$

Using the standard three-component scattering power decomposition technique [32], one can expand the measured coherency matrix $\mathbf{T}$ as a linear combination of three matrices corresponding to three mechanisms: 1) a rank-1 surface scattering ($\mathbf{T}_S$), 2) a rank-1 double-bounce scattering ($\mathbf{T}_D$), and 3) a rank-3 volume scattering ($\mathbf{T}_V$) matrices as,

$$\mathbf{T} = P_S\mathbf{T}_S + P_D\mathbf{T}_D + P_V\mathbf{T}_V \tag{4}$$

where, P_S, P_D and P_V are the expansion coefficients. $\mathbf{T}_S$, $\mathbf{T}_D$ and $\mathbf{T}_V$ are power-normalized matrices such that P_S, P_D and P_V represent the power contributions. These quantities must be non-negative, describing observable physical measurements for target scattering. However, the expansion coefficients often become negative for the Freeman-Durden 3-component method [32], which produces negative scattering power components.

Cui et al., [33] proposed an interesting technique to determine the non-negative expansion coefficients given in equation (4): P_S, P_D, and P_V. In order to do so, the volume scattering matrix $\mathbf{T}_V$ is first subtracted from $\mathbf{T}$ as,

$$\mathbf{T} - P_V\mathbf{T}_V = P_S\mathbf{T}_S + P_D\mathbf{T}_D \tag{5}$$

where $\mathbf{T}_S$ and $\mathbf{T}_D$ are rank-1 matrices. This suggests that $\mathbf{T} - P_V\mathbf{T}_V$ is, at most, a rank-2 matrix (i.e., its determinant must be zero).

$$\det(\mathbf{T} - P_V\mathbf{T}_V) = 0 \tag{6}$$

where $\det(\cdot)$ denotes the matrix determinant. One can note that equation (6) can be represented as a generalized eigendecomposition [34] problem as,

$$\mathbf{T}\mathbf{x} = \lambda\mathbf{T}_V\mathbf{x} \tag{7}$$

usually denoted as $\text{GEV}(\mathbf{T}, \mathbf{T}_V)$. The generalized eigenvalues (λ's) are always positive, and $\mathbf{x}$ is the associated eigenvector. Therefore, one can note that all the roots of equation (6) are always positive. The remainder matrix, $\mathbf{T}' = \mathbf{T} - P_V\mathbf{T}_V$ remains positive semidefinite, only for $P_V = \lambda_{\min}$, where $\lambda_{\min}$ is the minimum generalized eigenvalue obtained from equation (7). Hence, the volume scattering power is uniquely determined to be equal to the minimum root of equation (6).

The remainder matrix, $\mathbf{T}' = \mathbf{T} - P_V\mathbf{T}_V$ could be of the maximum rank of 2, and thus it might contain the contribution of up to two single scatterings. We determine them based on the fact that since $\mathbf{T}'$ is a positive-semidefinite matrix, we can directly express it as the sum of two rank-1 matrices as,

$$\mathbf{T}' = \lambda_1\mathbf{k}_1\mathbf{k}_1^{\dagger} + \lambda_2\mathbf{k}_2\mathbf{k}_2^{\dagger} \tag{8}$$

where, λ_1 and λ_2 are the eigenvalues of $\mathbf{T}'$, and the two eigenvectors $\mathbf{k}_1$ and $\mathbf{k}_2$ are orthogonal. Moreover, $\mathbf{k}_1$ denotes the dominant single scatterer when $\lambda_1 > \lambda_2$. Subsequently, we compute the scattering characterization parameter θ_{FP} to assess the dominant mechanism as either surface or double-bounce types. Then, accordingly, we consider the dominant surface scattering mechanism from the equation (8) for soil permittivity inversion.
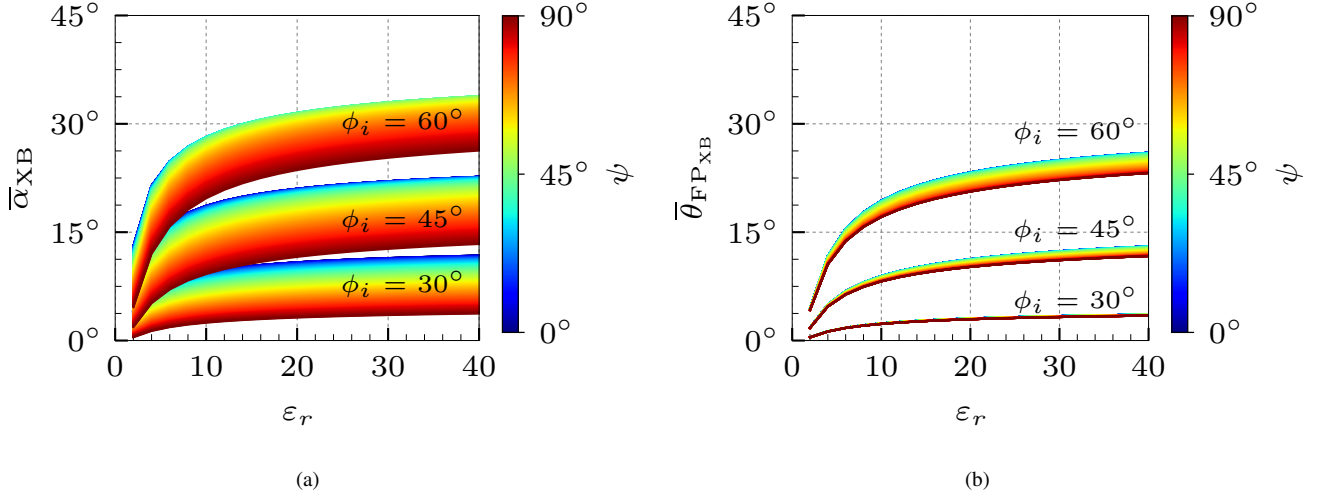
Fig. 1. Simulation plots for full polarimetry (a) $\overline{\alpha}_{\text{XB}}$ and (b) $\overline{\theta}_{\text{FP}_{\text{XB}}} = 45° - \theta_{\text{FP}_{\text{XB}}}$ as a function of the soil permittivity ε_r and surface roughness ψ at different local incidence angles ϕ_i.

1) Sensitivity Analysis of Scattering-type Parameters:
Cloude and Corr [12] demonstrated the sensitivity of the scattering-type parameter $\overline{\alpha}$ with soil permittivity for Bragg-type scatterers. Similarly, we have extended the study for the sensitivity of $\overline{\alpha}$ for the X-Bragg type of scatterers [11], [35].

One cannot neglect the presence of the cross-polarization term in surface scattering from rough agricultural surfaces. Therefore, the surface roughness-induced depolarization effect can be modeled using the X-Bragg model for such scenarios. From [14], the polarimetric coherency matrix for the X-Bragg model $\mathbf{T}_{\text{XB}}$ for the FP mode is expressed in equation (9) (provided at the bottom of the page).

In equation (9), f_s and β are surface scattering intensity and surface scattering mechanism ratio, respectively, and are defined as,

$$\beta = \frac{R_\parallel - R_\perp}{R_\parallel + R_\perp} \quad \text{and} \quad f_s = \frac{m_s^2}{2}|R_\parallel + R_\perp|^2 \qquad (10)$$

where $R_\parallel$ and $R_\perp$ are the horizontal and vertical Bragg scattering coefficients that depend on soil permittivity ε_r, and the local incidence angle ϕ_i as shown in equation (11). Here, m_s denotes the soil roughness influence on the surface intensity parameter f_s.

$$R_\parallel = \frac{\cos\phi_i - \sqrt{\varepsilon_r - \sin^2\phi_i}}{\cos\phi_i + \sqrt{\varepsilon_r - \sin^2\phi_i}}$$

$$R_\perp = \frac{(\varepsilon_r - 1)(\sin^2\phi_i - \varepsilon_r(1 + \sin^2\phi_i))}{(\varepsilon_r \cos\phi_i + \sqrt{\varepsilon_r - \sin^2\phi_i})^2} \qquad (11)$$

We can now express the scattering-type parameter $\overline{\alpha}$ for the X-Bragg model as,

$$\overline{\alpha}_{\text{XB}} = \frac{\lambda_{1_{\text{XB}}}\alpha_{1_{\text{XB}}} + \lambda_{2_{\text{XB}}}\alpha_{2_{\text{XB}}} + \lambda_{3_{\text{XB}}}\alpha_{3_{\text{XB}}}}{\lambda_{1_{\text{XB}}} + \lambda_{2_{\text{XB}}} + \lambda_{3_{\text{XB}}}} \qquad (12)$$

where $\lambda_{i_{\text{XB}}}$ is the ith eigenvalue and $\alpha_{i_{\text{XB}}} = \cos^{-1}(|\mathbf{e}_i|)$. Here, $\mathbf{e}_i$ is the ith eigenvector for the X-Bragg model. A detailed expression is provided in Appendix A.

The recently proposed target scattering-type parameter θ_{FP} [30] for FP data is expressed as,

$$\theta_{\text{FP}} = \tan^{-1}\left(\frac{m\,\text{Span}\,(T_{11} - T_{22} - T_{33})}{T_{11}\,(T_{22} + T_{33}) + m^2\,\text{Span}^2}\right) \qquad (13)$$

where m is the Barakat degree of polarization given in equation (14), and T_{ii} $(i = 1, 2, 3)$ are the diagonal elements of polarimetric coherency matrix, and Span is the total power.

$$m = \sqrt{1 - \frac{n^n|\mathbf{T}|}{\text{tr}^n(\mathbf{T})}} \qquad (14)$$

where $|\cdot|$ denotes the determinant, tr is the trace or total power and n is the dimension $\mathbf{T}$. For FP data, $n = 3$ in equation (14) and we designate $m_{\text{FP}} = m$.

Using equation (9) and equation (13), we now derive the expression of θ_{FP} for the X-Bragg model as,

$$\theta_{\text{FP}_{\text{XB}}} = \tan^{-1}\left(\frac{m_{\text{FP}_{\text{XB}}}\left(1 + |\beta|^2\right)\left(1 - |\beta|^2\text{sinc}(4\psi)\right)}{|\beta|^2 + m_{\text{FP}_{\text{XB}}}^2\left(1 + |\beta|^2\right)^2}\right) \qquad (15)$$

$$\mathbf{T}_{\text{XB}} = f_s \begin{bmatrix} 1 & \beta^* \,\text{sinc}\,(2\psi) & 0 \\ \beta\,\text{sinc}\,(2\psi) & \frac{1}{2}|\beta|^2(1 + \text{sinc}(4\psi)) & 0 \\ 0 & 0 & \frac{1}{2}|\beta|^2(1 - \text{sinc}(4\psi)) \end{bmatrix} \qquad (9)$$
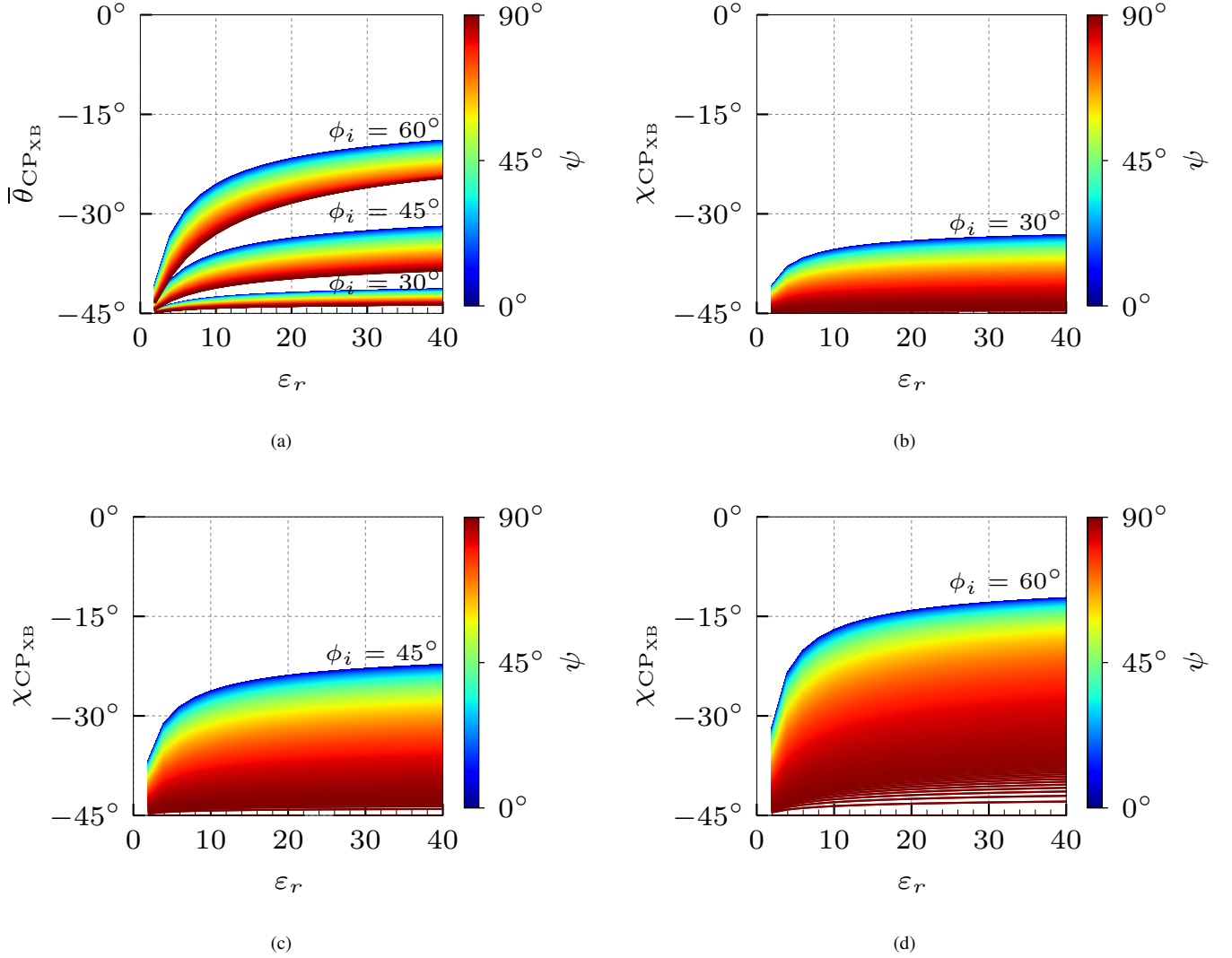
(a)

(b)

(c)

(d)

Fig. 2. Simulation plots for compact polarimetry (a) $\overline{\theta}_{\text{CP}_{\text{XB}}} = 45° - \theta_{\text{CP}_{\text{XB}}}$, (b)–(d) $\chi_{\text{CP}_{\text{XB}}}$ as a function of the soil permittivity ε_r and surface roughness ψ at different local incidence angles ϕ_i.

where $m_{\text{FP}_{\text{XB}}}$ is the 3D Barakat degree of polarization for the X-Bragg model expressed as a function of β and ψ as,

$$m_{\text{FP}_{\text{XB}}} = \left(1 - \frac{27|\beta|^4}{4(1+|\beta|^2)^3}\left[1 - \text{sinc}^2(4\psi)\right.\right.$$
$$\left.\left. + 2\text{sinc}^2(2\psi)\text{sinc}(4\psi) - 2\text{sinc}^2(2\psi)\right]\right)^{1/2} \quad (16)$$

Using the expressions given in equation (12) and (15), we conducted a sensitivity analysis to examine the variation of $\overline{\alpha}_{\text{XB}}$ and $\theta_{\text{FP}_{\text{XB}}}$ with soil permittivity (ε_r) and surface roughness descriptor (ψ). The sensitivity for $\overline{\alpha}_{\text{XB}}$ and $\theta_{\text{FP}_{\text{XB}}}$ for the X-Bragg model is shown in Figure 1. $\theta_{\text{FP}_{\text{XB}}}$ is scaled in Figure 1 and represented as $\overline{\theta}_{\text{FP}_{\text{XB}}} = 45° - \theta_{\text{FP}_{\text{XB}}}$ only for direct comparison.

One can observe that $\overline{\alpha}_{\text{XB}}$ is primarily influenced by ψ, especially at its higher values. On the contrary, $\theta_{\text{FP}_{\text{XB}}}$ is marginally affected by changes in ψ. Therefore, for typical croplands, the inversion of soil permittivity is less sensitive to the roughness condition while utilizing $\theta_{\text{FP}_{\text{XB}}}$. Hence, we use $\theta_{\text{FP}_{\text{XB}}}$ in forward modeling and, subsequently, for soil permittivity inversion as detailed in Section II-C.

B. Compact polarimetry

The hybrid compact polarimetric mode measures a projection of the 2×2 complex scattering matrix $\mathbf{S}$ as,

$$\begin{bmatrix} E_{CH} \\ E_{CV} \end{bmatrix} = \frac{1}{\sqrt{2}}\begin{bmatrix} S_{\text{HH}} & S_{\text{HV}} \\ S_{\text{VH}} & S_{\text{VV}} \end{bmatrix}\begin{bmatrix} 1 \\ \pm i \end{bmatrix}$$
$$= \frac{1}{\sqrt{2}}\begin{bmatrix} S_{\text{HH}} \pm iS_{\text{HV}} \\ S_{\text{VH}} \pm iS_{\text{VV}} \end{bmatrix}, \quad (17)$$

where the subscript C represents either left-hand $(+)$ or right-hand $(-)$ circular transmit. The 2×2 covariance matrix $\mathbf{C}_2$ is then obtained from the elements of the scattering vector as,

$$\mathbf{C}_2 = \begin{bmatrix} \langle |E_{CH}|^2 \rangle & \langle E_{CH}E_{CV}^* \rangle \\ \langle E_{CV}E_{CH}^* \rangle & \langle |E_{CV}|^2 \rangle \end{bmatrix}. \quad (18)$$

Similar to the FP mode, one can obtain a remainder covariance matrix $\mathbf{C}'$ using the generalized eigenvalue decomposition (GEV) technique for the observed $\mathbf{C}_2$ matrix along with the covariance matrix $\mathbf{C}_V = \mathrm{diag}(1,1)$ corresponding to the complete depolarization case (i.e., the degree of polarization is zero) as,

$$\mathbf{C}' = \mathbf{C}_2 - a\mathbf{C}_V \tag{19}$$

where $a = \min\{\lambda_1, \lambda_2\}$. Here, λ_1 and λ_2 are the generalized eigenvalues. As detailed in the following sections, we consider the dominant scattering mechanism from equation (19) for estimating soil permittivity.

1) Sensitivity analysis of scattering-type parameters: The X-Bragg model was proposed to accommodate surface-roughness induced depolarization in a surface scattering model [36]. As one cannot ignore the depolarization scattering phenomenon in the case of rough agricultural surfaces. Following this, one can express the Stokes vector elements as a function of the X-Bragg coherency matrix elements for compact polarimetric mode [29] as,

$$\begin{aligned} g_0 &= 0.5(C_1 + 2C_3), \quad g_1 = C_2 \operatorname{sinc}(2\psi) \\ g_2 &= 0, \qquad\qquad\quad g_3 = 0.5(C_1 - 2C_3) \end{aligned} \tag{20}$$

where ψ is the distribution width of the surface facet orientation angle, and C_1, C_2, and C_3 are the functions of the Bragg coefficients expressed as,

$$\begin{aligned} C_1 &= |R_\parallel + R_\perp|^2, \quad C_2 = (R_\parallel + R_\perp)(R_\parallel^* - R_\perp^*) \\ C_3 &= |R_\parallel - R_\perp|^2. \end{aligned} \tag{21}$$

One can note that $R_\parallel$ and $R_\perp$ depend on the dielectric constant ε_r and the incidence angle ϕ_i.

From [30], the scattering-type parameter θ_{CP} for CP data can be expressed as,

$$\theta_{\mathrm{CP}} = \tan^{-1}\left(\frac{m_{\mathrm{CP}}\, g_0\, (\mathrm{OC} - \mathrm{SC})}{\mathrm{OC} \times \mathrm{SC} + m_{\mathrm{CP}}^2\, g_0^2}\right), \tag{22}$$

where $\mathrm{OC} = (g_0 + g_3)/2$ and $\mathrm{SC} = (g_0 - g_3)/2$ describe the scattered power in the opposite sense transmitted and the same sense transmitted, respectively. For CP data, $n = 2$ in equation (14) and we designate $m_{\mathrm{CP}} = m$.

Therefore, the $\theta_{\mathrm{CP_{XB}}}$ for the hybrid polarimetric X-Bragg model can be expressed as,

$$\theta_{\mathrm{CP_{XB}}} = \tan^{-1}\left(\frac{m_{\mathrm{CP_{XB}}}\left(1 + |\beta|^2\right)\left(1 - |\beta|^2\operatorname{sinc}(4\psi)\right)}{\beta^2 + m_{\mathrm{CP_{XB}}}^2\left(1 + |\beta|^2\right)^2}\right) \tag{23}$$

where $m_{\mathrm{CP_{XB}}}$ is the 2D Barakat degree of polarization for the CP X-Bragg model as a function of β and ψ given as,

$$\begin{aligned} m_{\mathrm{CP_{XB}}} = \frac{2}{(\beta^2 + 1)}\Bigg(& 0.25\beta^4 + \beta^2 \operatorname{sinc}^2(2\psi) \\ & - 0.5\beta^2 + 0.25\Bigg)^{1/2} \end{aligned} \tag{24}$$

On the other hand, for the hybrid X-Bragg model, the wave ellipticity parameter, χ, can be expressed in terms of the Stokes vector elements ($\mathbf{g}_s = [g_0, g_1, g_2, g_3]$) as,

$$\chi_{\mathrm{CP_{XB}}} = 0.5\sin^{-1}\left(-\frac{g_3}{m_{\mathrm{CP_{XB}}} g_0}\right) \tag{25}$$

$$\begin{aligned} = 0.5\sin^{-1}\Bigg(& 0.5\beta^2 - 0.5\Big[0.25\beta^4 \\ & + \beta^2 \operatorname{sinc}^2(2\psi) - 0.5\beta^2 + 0.25\Big]^{-1/2}\Bigg) \end{aligned} \tag{26}$$

Now, using the expressions in equation (23) and equation (26), we perform a sensitivity study to examine the variation of $\chi_{\mathrm{CP_{XB}}}$ and $\theta_{\mathrm{CP_{XB}}}$ with soil permittivity (ε_r) and surface roughness descriptor (ψ). The sensitivity of $\theta_{\mathrm{CP_{XB}}}$ and $\chi_{\mathrm{CP_{XB}}}$ for the X-Bragg model is shown in Figure 2. $\theta_{\mathrm{CP_{XB}}}$ is scaled in Figure 2 and represented as $\overline{\theta}_{\mathrm{CP_{XB}}} = 45° - \theta_{\mathrm{CP_{XB}}}$ only for direct comparison. From Figure 2a, we can observe that the trend of $\theta_{\mathrm{CP_{XB}}}$ is similar to that of $\theta_{\mathrm{FP_{XB}}}$. However, the variation of $\chi_{\mathrm{CP_{XB}}}$ is comparatively higher with increasing value of ψ.

Therefore, $\chi_{\mathrm{CP_{XB}}}$ is more affected by ψ than $\theta_{\mathrm{CP_{XB}}}$, and therefore, for typical cropland, one can expect more robust soil permittivity estimation while utilizing $\theta_{\mathrm{CP_{XB}}}$ than $\chi_{\mathrm{CP_{XB}}}$. Therefore, we utilize $\theta_{\mathrm{FP_{XB}}}$ in the forward modeling and subsequently for soil permittivity inversion as detailed in Section II-C.

C. Inversion of soil permittivity

This study considers the X-Bragg surface scattering model as the forward model for both the full- and compact-pol modes. We selected the X-Bragg model to understand the effect of surface roughness induced depolarization on soil moisture inversion.

The model derived surface scattering mechanisms $\theta_{\mathrm{FP_{XB}}}$ and $\theta_{\mathrm{CP_{XB}}}$ are further utilized in the inversion. We performed the inversion by comparing modeled scattering-type parameter and the dominant surface scattering-type parameter derived from the observed data (as explained in Sections II-A and II-B).

We use a simple 1D minimum operator to retrieve the corresponding dielectric constant of the soil, i.e., $\min_{\varepsilon_r}\left(|\theta_{\mathrm{FP_{XB}}} - \theta_{\mathrm{FP_{data}}}^{\mathrm{dominant}}|\right)$ for FP data and $\min_{\varepsilon_r}\left(|\theta_{\mathrm{CP_{XB}}} - \theta_{\mathrm{CP_{data}}}^{\mathrm{dominant}}|\right)$ for CP data. One should note that the inversion of soil permittivity is obtained only for pixels with dominant soil contribution, i.e., $\theta_{\mathrm{FP_{data}}}^{\mathrm{dominant}}$ or $\theta_{\mathrm{CP_{data}}}^{\mathrm{dominant}} > 30°$. A schematic flow of the proposed methodology is shown in Figure 3. We divided the schematic flow into two major steps: 1) pre-processing: which includes extraction of the dominant scattering mechanism for both FP and CP SAR configurations, and 2) soil permittivity estimation from the dominant scattering mechanism (the shaded portion in Figure 3).

III. STUDY AREA AND EXPERIMENTAL DATA

A. Study Area

We used the SMAPVEX12 experimental area as our study site, which covers an area of $15\,\mathrm{km} \times 70\,\mathrm{km}$. It is situated in Winnipeg, Canada, near the foot of the Red River watershed.

Extraction of dominant scattering mechanism

Soil permittivity inversion

UAVSAR data

$\mathbf{T}_3$

FP

$P_r = 10log_{10}(S_{VV}S_{VV}^* S_{HH}S_{HH}^*)$

Random/Vertical/Horizontal

$\{\lambda_1,\ \lambda_2,\ \lambda_3\} = \text{GEV}(\mathbf{T}_3, \mathbf{T}_V)$

$a = \min\{\lambda_1,\ \lambda_2,\ \lambda_3\}$

$\mathbf{T}' = \mathbf{T}_3 - a\mathbf{T}_V$

Eigen Decomposition
$\mathbf{T}' = \lambda_1 \mathbf{k}_1 \mathbf{k}_1^\dagger + \lambda_2 \mathbf{k}_2 \mathbf{k}_2^\dagger$

(A)

CP

$(\text{Compact } \mathbf{C}_2)_{\chi=45°,\ \varphi=0°}$

$\mathbf{C}_V = $ Complete depolarizer

$\{\lambda_1,\ \lambda_2\} = \text{GEV}(\mathbf{C}_2, \mathbf{C}_V)$

$a = \min\{\lambda_1,\ \lambda_2\}$

$\mathbf{C}' = \mathbf{C}_2 - a\mathbf{C}_V$

Stokes parameterization of $\mathbf{C}'$

(A)

(A)

First dominant scattering mechanism

$\theta_{\text{FP/CP}}^{\text{dominant}} > 30°$ — N → Non-invertible

Y

Surface dominant scattering

$\theta_{\text{FP/CP}}^{\text{XB}}$ from X-Bragg model

$\min_{\varepsilon_r} \left(|\theta_{\text{FP/CP}}^{\text{XB}} - \theta_{\text{FP/CP}}^{\text{dominant}}| \right)$
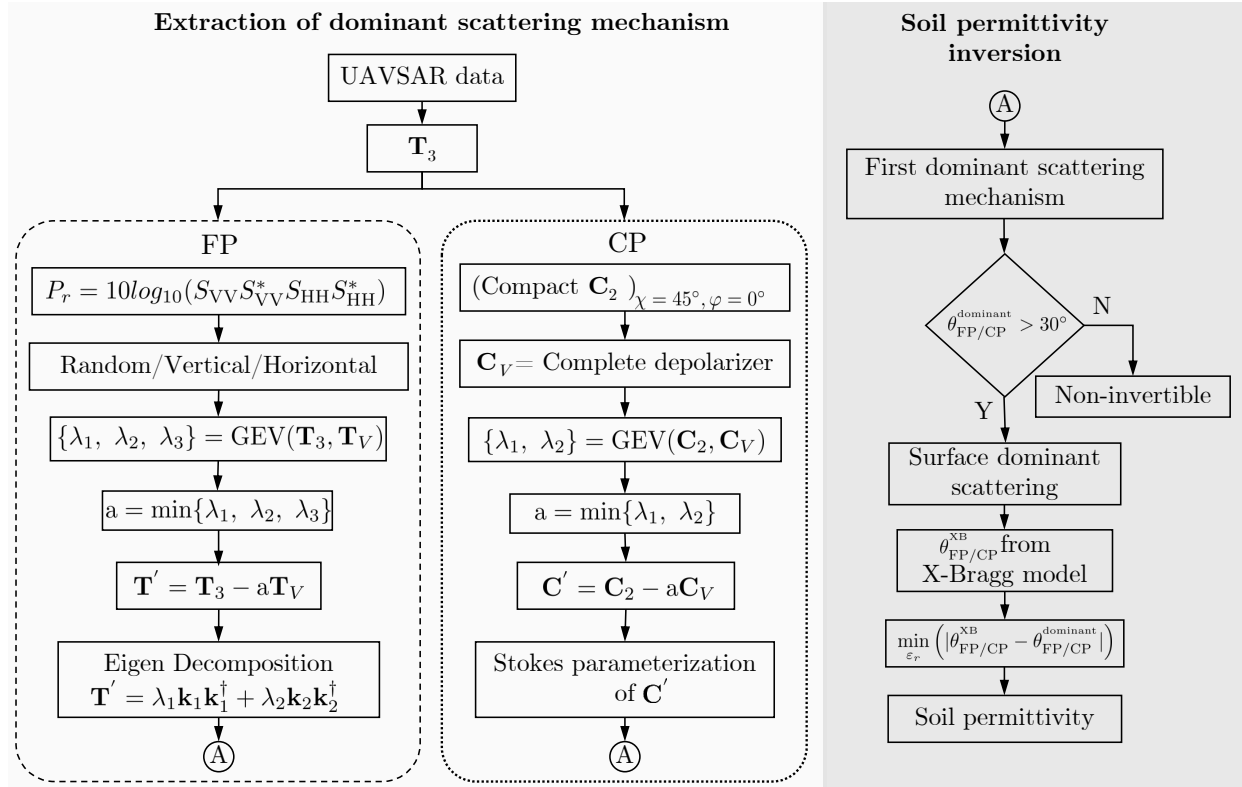
Soil permittivity

Fig. 3. Flow chart of the methodology for soil permittivity estimation from full- and compact-pol SAR data. Here (A) indicates the break point between the pre-processing step and the soil permittivity estimation step.
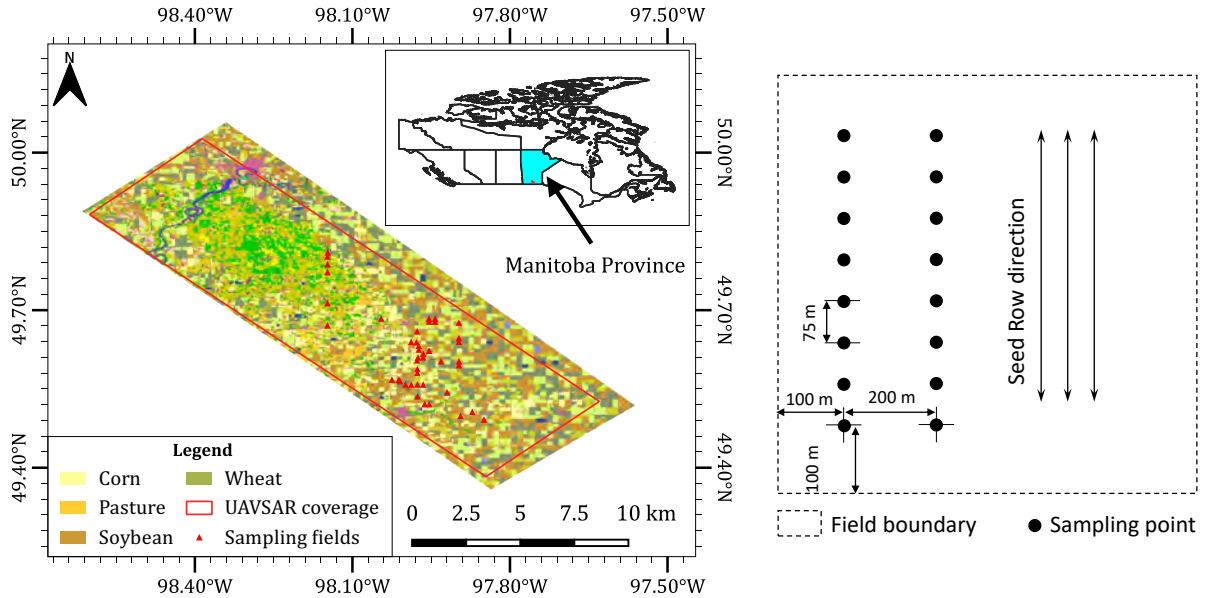

Fig. 4. Left: Map showing the locations of the sampling fields and crop map of the study area. UAVSAR scene coverage for flight Line ID: #31606 is overlaid as a red polygon. Right: The sampling schema followed to acquire soil permittivity values for each field.

The region has a humid continental climate and receives annual precipitation of approximately $505\,\text{mm}$. It consists of agricultural, forests, and pasture lands. A highly flat topography characterizes the landscape. Major crops grown in the agricultural area are wheat, canola, soybean, and corn. We have provided a map of the study area with locations of the sampling fields in Figure 4.

B. UAVSAR time series

During the SMAPVEX12 campaign, 14 L-band polarimetric UAVSAR scenes are acquired between June 17 and July 17,
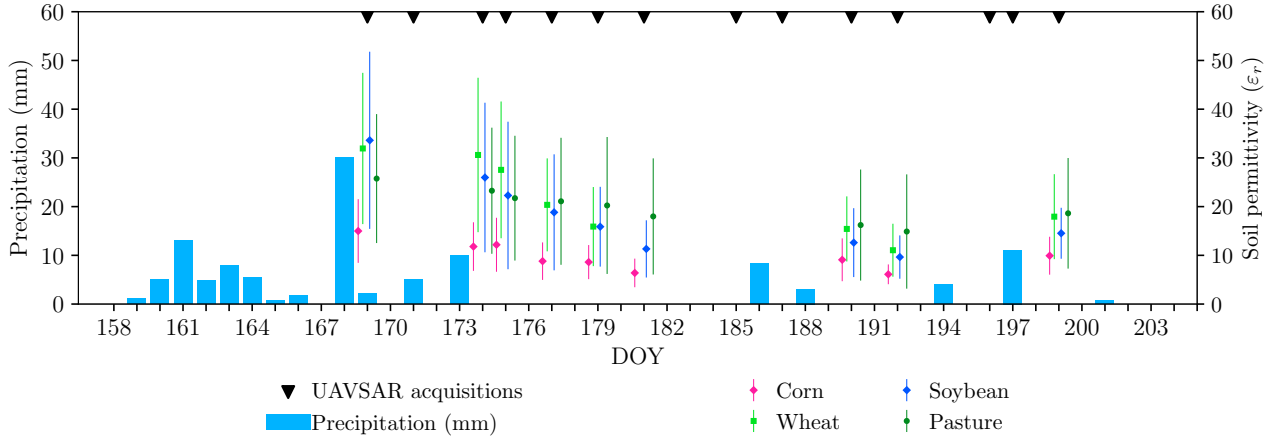
Fig. 5. Time-series plot of soil permittivity (mean $\pm$ standard deviation) for different crops. Daily precipitation values (blue bars) from the meteorological station within the study area and the UAVSAR acquisition days are also presented [37].

TABLE I

SPECIFICATIONS OF UAVSAR DATA (FULL-POL/MLC GRD) USED IN THIS STUDY (FLIGHT LINE ID: #31606) ALONG WITH CORRESPONDING DATES OF IN-SITU MEASUREMENTS.

Day of Year (DOY)	Date of SAR data acquisition	Flight ID	Range of incidence angle (Deg.)	Date of In-situ measurements
169	6/17/2012	12044	22.59-65.18	6/17/2012
174	6/23/2012	12046	22.73-66.32	6/23/2012
175	6/24/2012	12047	21.32-65.42	6/24/2012
177	6/25/2012	12048	21.38-66.68	6/25/2012
179	6/27/2012	12049	22.83-67.42	6/27/2012
181	6/29/2012	12050	21.31-65.52	6/29/2012
185	7/03/2012	12055	21.34-66.14	7/03/2012
187	7/05/2012	12056	22.56-65.83	7/05/2012
190	7/08/2012	12057	22.25-66.61	7/08/2012
192	7/10/2012	12058	22.54-66.16	7/10/2012
195	7/13/2012	12059	22.54-66.16	7/13/2012
196	7/14/2012	12060	22.54-66.16	7/14/2012
199	7/17/2012	12061	21.45-66.52	7/17/2012

C. Ground measurements

Extensive field measurements were collected during the SMAPVEX12 campaign, with near synchronous UAVSAR acquisitions over 55 agricultural fields. The collection of field measurements spans between 6th June and 17th July 2012. Both the soil and vegetation characteristics are measured during this field campaign. Soil permittivity was measured using the hand-held Hydra probes at an average depth of $5\,\mathrm{cm}$. Three replicate measurements were made to get a representative soil permittivity value for each point. Likewise, sixteen locations were selected for each field to sample soil permittivity. The daily rainfall was also noted to evaluate soil permittivity dynamics. There is a good agreement between the temporal evolution of the mean soil permittivity measurements and the amount of rainfall, as shown in Figure 5. Usually, a peak in the mean soil permittivity value follows a precipitation event. It then follows a quasi-exponential decrease in the absence of irrigation, precipitation and/or evaporation (Figure 5). One can find more details about these measurements in [40].

2012. The incidence angle varies between $25°$ to $65°$ with a nominal swath of $21\,\mathrm{km}$. This study uses a multi-look complex (MLC) product acquired for the flight line #31606. This flight line covers all the investigated agricultural fields. A spatial resolution of $5.0\,\mathrm{m}$ in range and $7.2\,\mathrm{m}$ in azimuth are considered. We extracted the coherency matrix $\mathbf{T}$ and speckle-filtered them with the refined Lee filter with a window size of 5×5 using PolSARpro software. As the terrain is flat, we need not apply any topographic correction technique.

We simulated the compact-pol data from the UAVSAR full polarimetric data. The compact polarimetric 2×2 covariance matrix $\mathbf{C}_2$ is obtained from the 3×3 full polarimetric covariance matrix $\mathbf{C}_3$ considering the right circular transmit configuration, i.e., ellipticity, $\chi = -45°$ and orientation angle, $\varphi = 0°$ to simulate the datasets [38]. Subsequently, the scattering type parameters are extracted using the PolSAR tools plugin [39].

IV. RESULTS AND DISCUSSION

First, we extract and analyze the entropy and scattering-type parameters from UAVSAR L-band data for FP and CP SAR configurations. We have examined the data collected over the SMAPVEX-12MB test site for four crops (corn, pasture, soybean, and wheat) throughout the major phenological stages. In Section II, we have evaluated the theoretical sensitivity of the extracted scattering-type parameters from full and compact polarimetric data. We now focus on the inversion of soil permittivity. We assessed the agreement between the in-situ and estimated soil permittivity values using the Pearson correlation coefficient r and Root Mean Square Error (RMSE). The subsequent sections present the analysis details for full and compact SAR data.
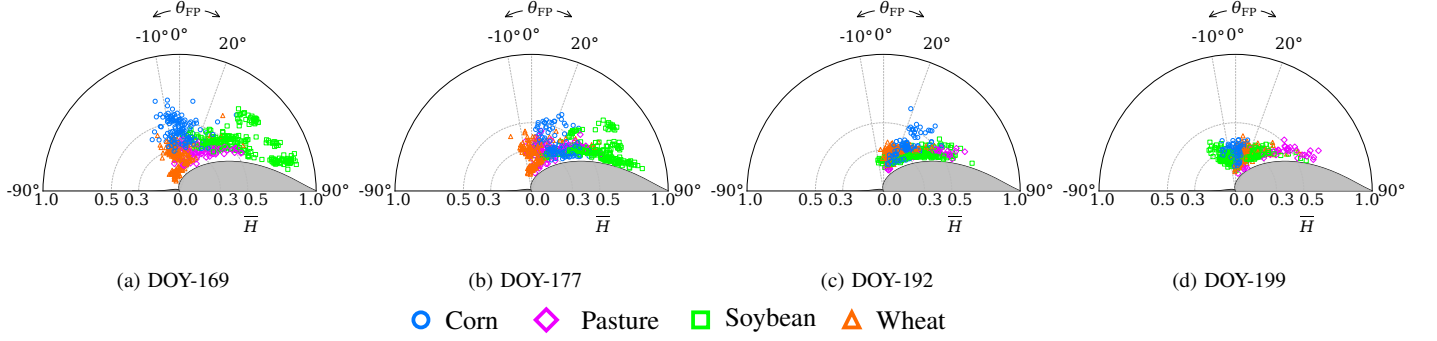
Fig. 6. Temporal $\overline{H}/\theta_{\mathrm{FP}}$ plots derived for various crops. $\overline{H} = 1 - \mathrm{Entropy}(H)$ i.e. $\overline{H} = 0$ corresponds to high entropy and $\overline{H} = 1$ corresponds to low entropy. Similarly, $\theta_{\mathrm{FP}} = -90°$, $0°$ and $90°$ represents pure dihedral, random (depolarized) and trihedral type of scattering respectively. Note that θ_{FP} is scaled by a factor of 2 for representation. No scattering mechanisms exist in the shaded portion. For a detailed interpretation of the plot, see [41].
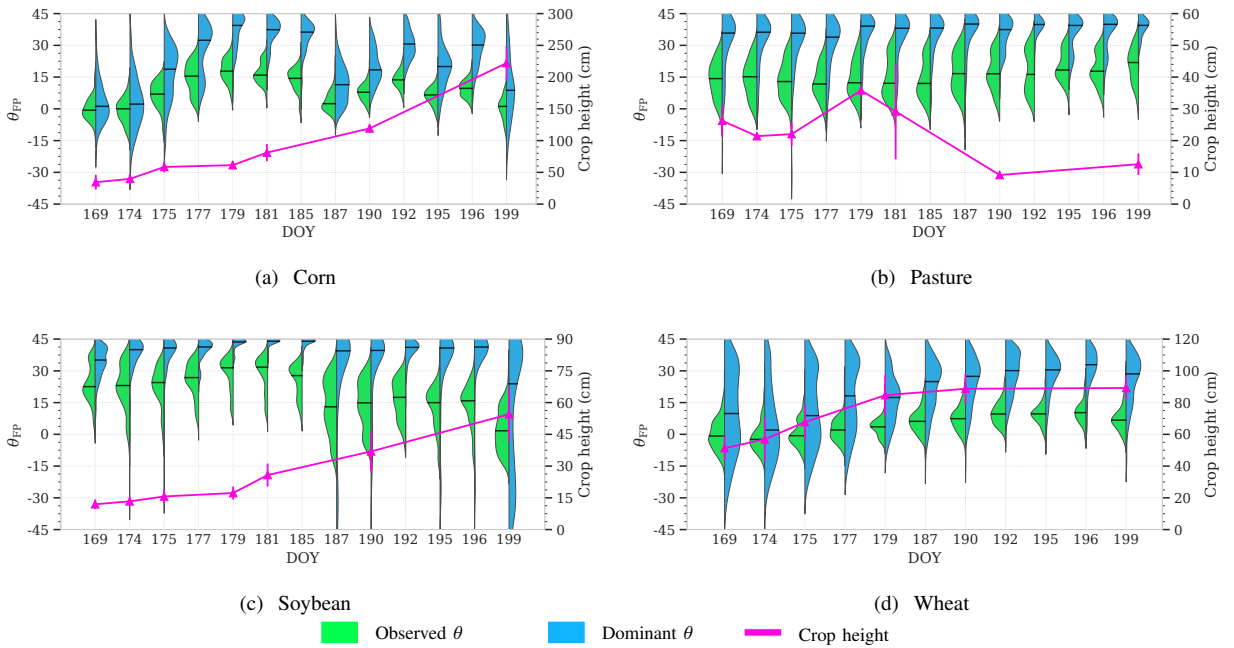

Fig. 7. Temporal evolution of observed and dominant scattering mechanism over various crops. These violin plots represent the kernel density estimation displaying the shape of the data distribution along with the median value. The secondary y-axis shows the mean±standard deviation of crop height for each crop type.

A. Full polarimetry

This section details the analysis of the proposed approach for full polarimetric UAVSAR data, followed by a comparative study of the estimates from two scattering-type parameters for the four crop types mentioned above.

We first analyze the temporal dynamics of entropy-scattering type parameter using the $\overline{H}/\theta_{\mathrm{FP}}$ clustering plane over these crops (note that, here $\overline{H} = 1 - H$, where H is the scattering entropy). We chose four acquisitions temporally 1-2 weeks apart to analyze changes in scattering mechanism and entropy during the observation period (Figure 6). During the initial vegetation growth period on DOY-169, we observe low entropy and high θ_{FP} values (Figure 6a) for corn, pasture, and soybean due to sparse vegetation structure and considerable contribution from the soil. However, for wheat, we observe medium to

higher entropy and low θ_{FP} values due to higher canopy height (>50 cm). One can note that $\overline{H}$ values are relatively higher (0.56) for soybean than other crops. These relatively high $\overline{H}$ values are due to the low canopy height of $10.67 \, \mathrm{cm}$ during DOY-169. In addition, the moderate canopy heights of corn and pasture produced higher values of $\overline{H}$. On the contrary, the mean canopy height of wheat ($> 50 \, \mathrm{cm}$) produced $\overline{H} = 0.12$ indicating higher entropy.

We also observe a shift in the clusters from low to high entropy zones from DOY-169 to DOY-199. This shift typically indicates a decrease in $\overline{H}$ values due to the increase in canopy height and foliage density. Additionally, we observe a change in the scattering mechanism from odd to even multiple-bounce over soybean fields in Figure 6d. This shift in the scattering mechanisms might be due to increased crop stem diameter and
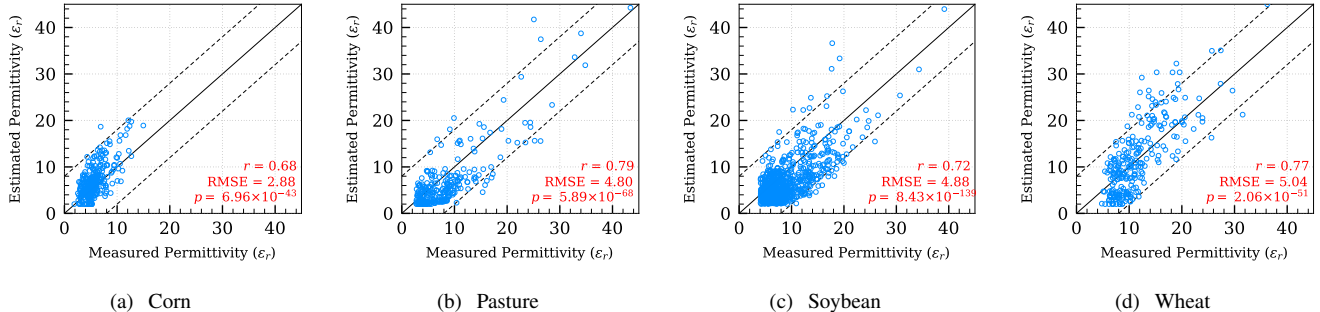
Fig. 8. Scatter plots of measured soil permittivity and estimated soil permittivity for different crops using scattering mechanism $\overline{\alpha}$. The solid line represents the 1:1 line, and the dashed lines denotes ± 8 offset from the 1:1 line.
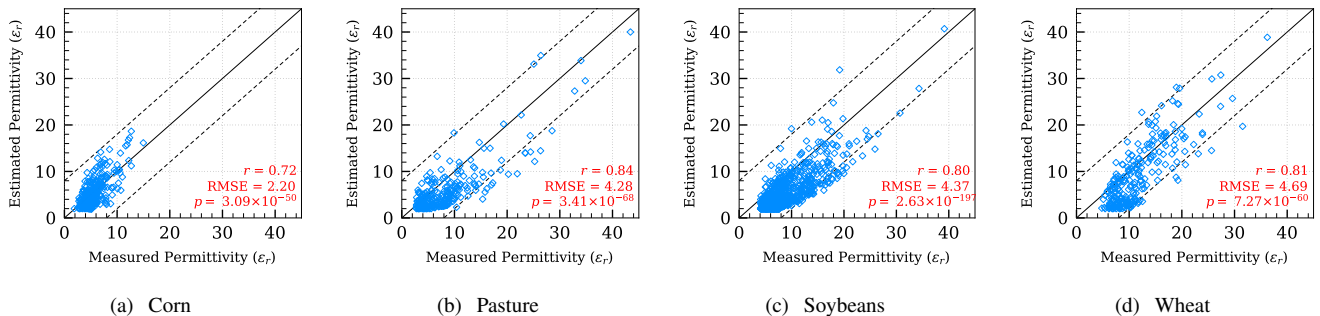

Fig. 9. Scatter plots of measured soil permittivity and estimated soil permittivity for different crops using scattering mechanism θ_{FP}. The solid line represents the 1:1 line, and the dashed lines denotes ± 8 offset from the 1:1 line.

soil permittivity due to the preceding rainfall event on DOY-197. On the contrary, we observe an increase $\overline{H}$ for pasture due to a decrease in canopy height from approximately $30\,\text{cm}$ on DOY-181 to $10\,\text{cm}$ on DOY-199.

Figure 7 shows the temporal changes of observed and dominant scattering mechanisms for FP SAR (derived as detailed in Section II-A). Thus we observe that most of the dominant θ values are towards odd bounce (surface) scattering. As shown in Figure 7a, for corn, till DOY-174 (canopy height $< 50\,\text{cm}$) we observe a strong volume scattering (dominant $\theta \approx -0.70° \pm 6.1°$). This volume scattering dominance could be because of wet stubbles and surface roughness. However, from DOY-177, the dominant scattering shifted to surface and mixed volume. Further, increase in canopy height of more than $200\,\text{cm}$ on DOY-199 generated more volume scattering (dominant $\theta \approx 0.43° \pm 5.3°$). In the case of pasture (Figure 7b), due to low canopy height ($< 40\,\text{cm}$) and density, the dominant scattering mechanism remains surface for the entire observation period.

Similarly, for soybean, the dominant scattering mechanism is surface due to low canopy height of $< 50\,\text{cm}$ till DOY-196. However, during DOY-199, we observe a bimodal distribution (Figure 7c) of dominant θ, indicating both even and odd bounce scattering. This bimodal nature could be because of increased canopy density and rainfall events on DOY-197. For wheat (Figure 7d), we observe dominant volume scattering during the initial dates (DOY-169 to DOY-175), which is similar to what we observe for corn. However, the dominant mechanism shifted towards the surface from DOY-177.

We utilize the dominant surface scattering mechanism analysis in the previous paragraphs to estimate soil permittivity. We show the scatter plots of measured soil permittivity compared with estimated soil permittivity from the developed inversion approach using $\overline{\alpha}$ and θ_{FP} in Figures 8 and 9, respectively. From the in-situ measurements, the overall dynamic range of measured soil permittivity is from 3 to 45. Further, we obtain the lowest RMSE of 2.2 with a r value of 0.72 for corn with θ_{FP} as presented in Figure 9a. This low RMSE in both θ_{FP} and $\overline{\alpha}$ estimates could be due to less overall dynamic range of measured permittivity over corn (maximum $\varepsilon_r = 14.97$). It is important to note that we obtain an improvement of $\approx 21.4\,\%$ RMSE when we use θ_{FP} compared to that of $\overline{\alpha}$. One of the major reasons for these differences in estimates could be the residual depolarizing component in the dominant scattering because of corn canopy height and structure and also due to the sensitivity of parameters as shown in Figure 1.

For the other three crops (viz., pasture, soybean, and wheat), we obtain RMSE in the range of $4 - 5$ with θ_{FP}. Despite their lower height than corn, there is an increase in RMSE for these three crops. One of the major reasons for this observation is the lower sensitivity of the X-Bragg model for high permittivity and a higher dynamic range of soil permittivity. Several previous researchers also observed and reported this decrease in sensitivity of the X-Bragg model with an increase in permittivity [15], [36]. Due to this reason, one can observe higher uncertainty in estimates with the increase in permittivity. Nevertheless, we obtain a $10.5\,\%$ improvement in RMSE for pasture and soybean with θ_{FP}.
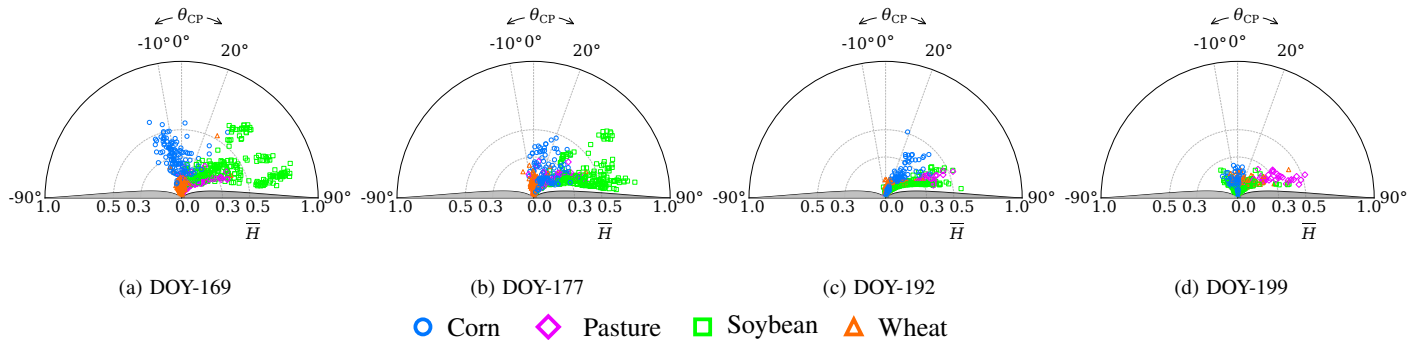
(a) DOY-169 **(b) DOY-177** **(c) DOY-192** **(d) DOY-199**

○ Corn   ◇ Pasture   □ Soybean   △ Wheat

Fig. 10. Temporal $\overline{H}/\theta_{CP}$ plots derived for various crops. $\overline{H} = 1 - \text{Entropy}(H))$ i.e. $\overline{H} = 0$ corresponds to high entropy and $\overline{H} = 1$ corresponds to low entropy. Similarly, $\theta_{CP} = -90°$, $0°$ and $90°$ represents pure dihedral, random (depolarized) and trihedral type of scattering respectively. Note that θ_{CP} is scaled by a factor of 2 for representation. No scattering mechanisms exist in the shaded portion. A detailed description of the plot is given in [41]).

(a) Corn **(b) Pasture**

(c) Soybean **(d) Wheat**

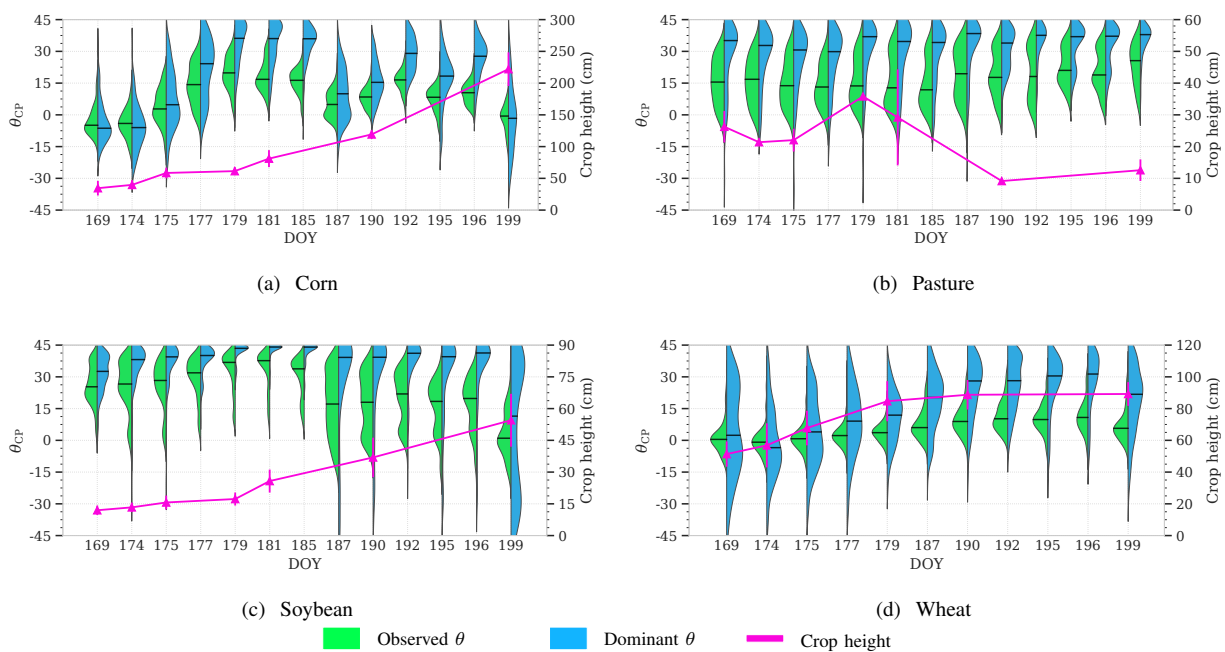■ Observed θ ■ Dominant θ — Crop height

Fig. 11. Temporal evolution of observed and dominant scattering mechanism over various crops. These violin plots represent the kernel density estimation displaying the shape of the data distribution along with the median value. The secondary y-axis shows the mean±standard deviation of crop height for each crop type.

Furthermore, one can observe a noticeable spread of estimated permittivity values in wheat using $\overline{\alpha}$. This spread might be because of a high crop canopy height of $> 50\,\text{cm}$ from DOY-169. Wheat fields were in the heading and flowering stage from DOY-169 to DOY-190 [37], [42]. During this phenology stage, one can observe increased depolarization of the scattered wave [43]. Therefore, a residual depolarizing component in the dominant scattering could explain high uncertainty in estimates from $\overline{\alpha}$. In contrary, we obtain a $7\,\%$ better accuracy with θ_{FP}. In summary, we obtain an improvement of $7\,\%$ to $20\,\%$ RMSE with the proposed method for FP SAR data. We have detailed the performance metrics derived from the developed algorithm in Table II.

TABLE II
SUMMARY OF VALIDATION ACCURACY METRICS OF THE PROPOSED INVERSION METHODOLOGY FOR VARIOUS CROPS USING FP SAR DATA ($r-$ PEARSON CORRELATION COEFFICIENT AND RMSE$-$ROOT MEAN SQUARE ERROR).

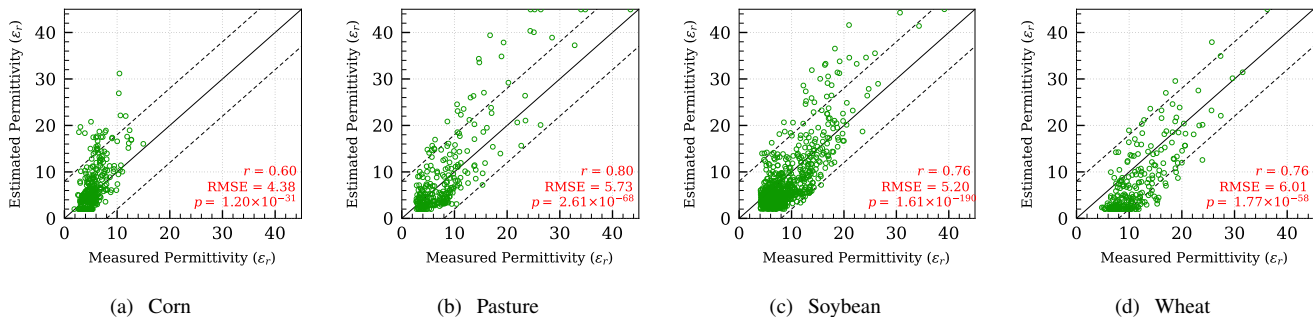| **Crop Type**	$\overline{\alpha}$		θ_{FP}	
	r	RMSE	r	RMSE
Corn	0.68	2.88	0.72	2.20
Pasture	0.79	4.80	0.84	4.28
Soybean	0.72	4.88	0.80	4.37
Wheat	0.77	5.04	0.81	4.69

Fig. 12. Scatter plots of measured soil permittivity and estimated soil permittivity for different crops using χ. The solid line represents the 1:1 line, and the dashed lines denote ± 8 offset from the 1:1 line.
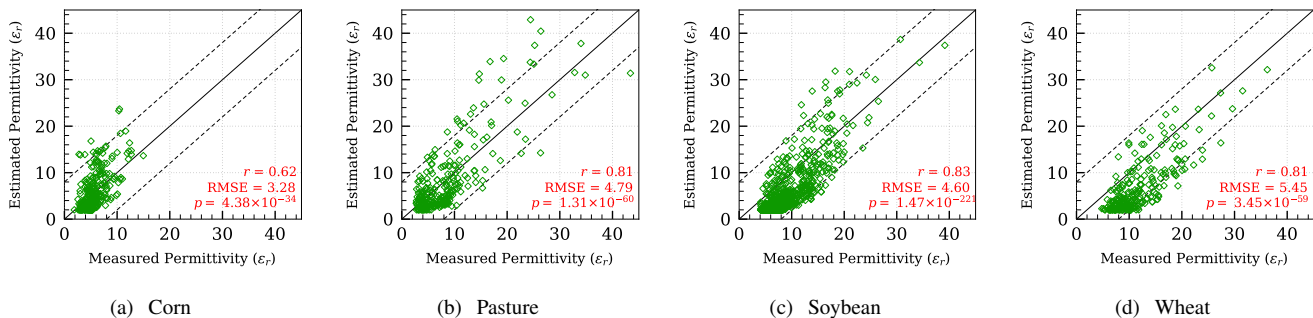

Fig. 13. Scatter plots of measured soil permittivity and estimated soil permittivity for different crops using θ_{CP}. The solid line represents the 1:1 line, and the dashed lines denotes ± 8 offset from the 1:1 line.

B. Compact polarimetry

This section details the analysis of the proposed approach for simulated compact polarimetric UAVSAR data. We have simulated hybrid-CP SAR data with the right circular transmit configuration, i.e., $\chi = -45°$ and $\varphi = 0°$ [38]. We provide a comparative study of the estimates from two scattering-type parameters for the four crops mentioned above types.

Similar to FP data, we first analyze the temporal dynamics of entropy-scattering type parameter using the $\overline{H}/\theta_{\text{CP}}$ clustering plane over these crops as shown in Figure 10. During the initial vegetation growth period on DOY-169, lower entropy and higher θ_{CP} values are observed due to lower canopy height, as shown in Figure 10a. The temporal trend of clusters is similar to FP, with a few minor differences. During DOY-169, we observe relatively lower θ_{CP} values in the case of corn (i.e., towards a mixture of volume and multiple even bounce) compared to that of FP. Further, we observe a relatively higher entropy for all four crops due to similar preferences in all the scattering eigenstates in the case of CP SAR data.

Figure 11 shows the temporal changes of observed and dominant scattering mechanisms for CP SAR data (extracted as detailed in Section II-B). The temporal trend and the distribution of dominant θ_{CP} follows that of dominant θ_{FP}. Moreover, the majority of the dominant θ_{CP} values are towards the odd-bounce (surface) scattering. For corn, we observe lower values of θ_{CP} along with a marginal increase in standard deviation compared to that of θ_{FP}. For example, in the case of corn on DOY-169: $\theta_{\text{FP}} = 0.01° \pm 5.62°$, $\theta_{\text{CP}} = -2.71° \pm 7.16°$

as shown in Figures 7a, 11a. In contrast, for pasture, we observe higher θ values along with increased standard deviation in CP compared to that of FP.

These contrasting values of θ for different crops are majorly due to the decrease in the Barakat DOP for CP data. For instance, at L-band, attenuation due to $< 50\,\text{cm}$ of pasture canopy is significantly low compared to that of corn with canopy height $> 100\,\text{cm}$. Interestingly, we observed higher θ values for CP data for soybean than FP. For instance, as shown in Figures 11c and 7c, at $40\,\text{cm}$ of canopy height during DOY-190, $\theta_{\text{CP}} = 17.54° \pm 13.58°$ whereas $\theta_{\text{FP}} = 14.08° \pm 11.26°$. Moreover, we observe lower values for dominant θ for CP data by order of $2°$ to $3°$, which might be due to the decrease in the Barakat DOP.

We utilize this dominant scattering-type parameter θ_{CP} for the inversion of soil permittivity. We presented the obtained scatter plots of measured soil permittivity compared with estimated soil permittivity from the developed inversion approach using χ and θ_{CP} in Figures 12 and 13 respectively. Comparing the permittivity inversion results from χ and θ_{CP}, we observe better accuracy by θ_{CP} for all the four crops.

However, the RMSE values are marginally high for CP than in FP due to the reduced information in CP. For corn, we obtain an RMSE of 3.28 with θ_{CP}, whereas with χ, we get a higher RMSE of 4.38. It is interesting to note that most of the permittivity estimates from χ are greater than that of θ_{CP}. These higher values could be because of the effect of the roughness descriptor on χ than θ. As shown in the simulation study, a high dynamic range of χ values for a given permittivity value
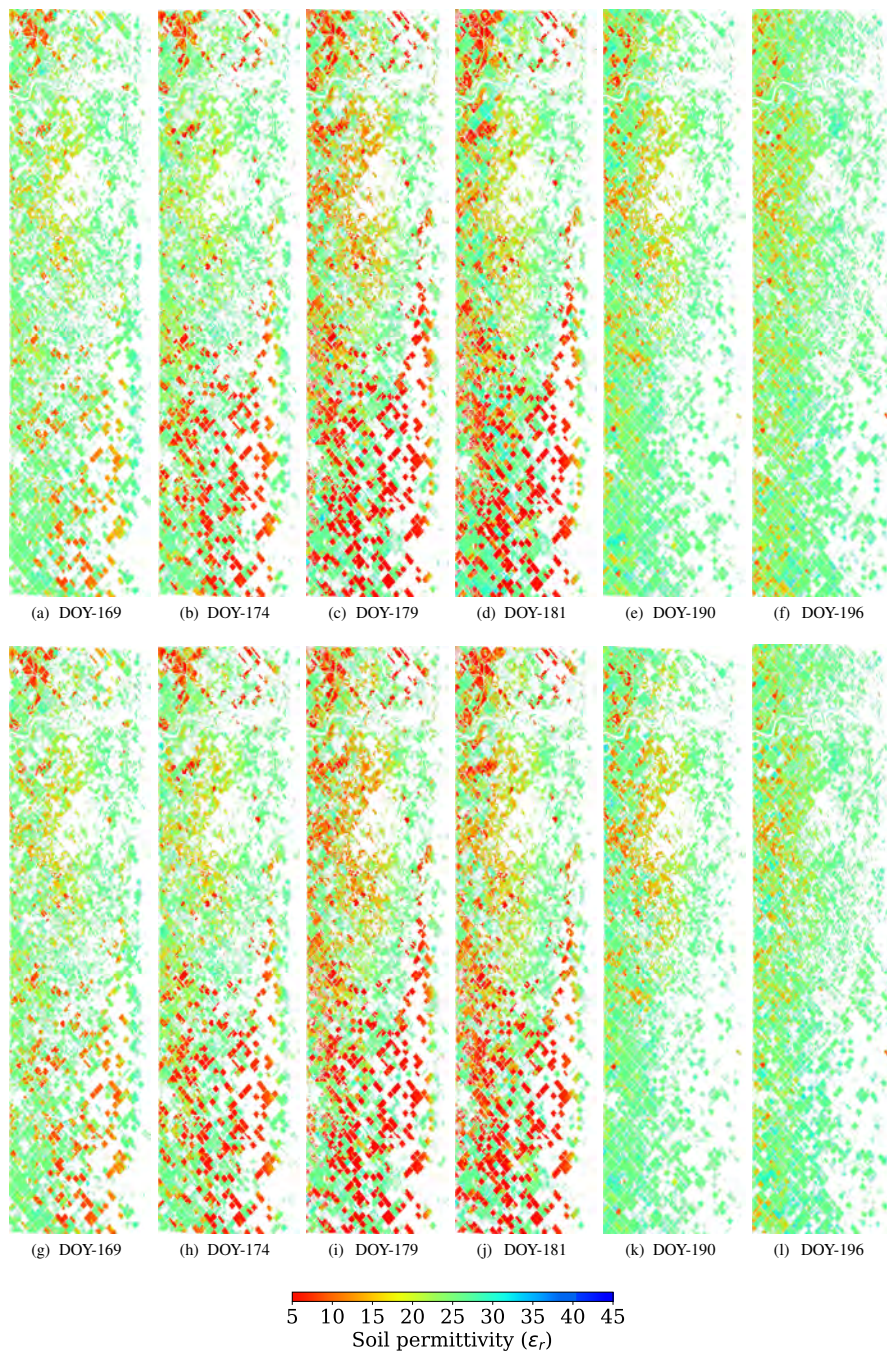
Fig. 14. Spatiotemporal maps of the estimated soil permittivity derived from FP (top row) and CP (bottom row) SAR data over the test site for various temporal acquisitions, near range to far range runs from left to right within the images.

(Figure 2) might produce a high uncertainty in the estimates from χ than θ_{CP}.

A similar overestimation phenomenon is also observed in the case of pasture, as seen in Figure 8b. Moreover, we observe that the estimates from a few points have reached a maximum permittivity value. The overestimation could be because of the increased surface roughness due to the harvesting processes [44], as one can observe that the pasture fields were harvested between DOY-181 and DOY-190 from Figure 11b. Therefore, we obtain a high RMSE of 5.73 with χ. There is

also a marginal overestimation with θ, which is relatively less with an RMSE of 4.79.

For soybean, we obtain an improvement of 11.5% RMSE with θ_{CP} compared to that of χ. In the case of wheat, we obtain an RMSE of 5.45 with θ_{CP}, whereas with χ, we obtain a higher RMSE of 6.01. In summary, we obtain an improvement of 9% to 25% RMSE with the proposed method for CP SAR data. The performance metrics derived from the developed algorithm for CP SAR data are detailed in Table III.

Soil permittivity maps derived from FP and CP SAR data

TABLE III
SUMMARY OF VALIDATION ACCURACY METRICS OF THE PROPOSED
INVERSION METHODOLOGY FOR VARIOUS CROPS USING CP SAR DATA (r−
PEARSON CORRELATION COEFFICIENT AND RMSE−ROOT MEAN SQUARE
ERROR).

Crop Type	χ		θ_{CP}	
	r	RMSE	r	RMSE
Corn	0.60	4.38	0.62	3.28
Pasture	0.80	5.73	0.81	4.79
Soybean	0.76	5.20	0.83	4.60
Wheat	0.76	6.01	0.81	5.45

over the test site are presented in Figure 14. The overall temporal trend of estimated soil permittivity agrees with field measurements and rainfall events. For instance, from in-situ data in Figure 5, we can observe a quasi-exponential decreasing trend in soil permittivity from DOY-169 to DOY-182. Therefore, a similar dynamic range and spatial distribution of estimated soil permittivity are observed in Figure 14. The rainfall events after DOY-185 lead to an increase in soil permittivity, which we can notice as an increase in permittivity estimates on DOY-190 and DOY-196 in Figure 14. Despite the high similarity between the permittivity maps derived from FP and CP SAR data, we record a relatively marginal overestimation of soil permittivity with CP SAR. This overestimation could be due to reduced information in CP mode and the effect of increased entropy.

We observe the effect of variability of the incidence angle from near to far range on the soil permittivity inversion. Specifically, this incidence angle effect is more evident in advanced crop phenology. This is because, in forward modeling of the surface component, the incidence angle influences the calculus of the decomposed surface scattering-type parameters, consequently affecting soil permittivity inversion [16]. Therefore, we minimize this effect by using the local incidence angle (ϕ_i), which includes the terrain slopes, in the inversion process for the X-Bragg model. Furthermore, it is observed that low incidence angles provide more valid pixels for the retrieval process, with a compromise of the decreased sensitivity of θ_{FP} or $\overline{\alpha}$ to soil dielectric constant (Figure 1). A similar observation was also reported in the previous studies [9], [15], [19].

We performed a field scale analysis with four sample fields (one for each crop) to study the spatial and temporal viability of soil permittivity, as shown in Figure 15. The quantitative summary of estimates is shown in Table IV. Overall we observe that the temporal variation of the estimated soil permittivity is in good agreement with rainfall data and in-situ measurements. Further, one can notice that the estimation rate is considerably high ($\geq 80\,\%$) for all four crops throughout the observation period. Furthermore, the permittivity estimates from FP data and CP data are in accordance with each other, indicating the robustness and generalizability of the proposed method. In summary, the quantitative and qualitative soil permittivity estimates from the proposed method (for both FP and CP SAR modes) conform with the in-situ measurements.

(a) Corn (Field ID: 83)

(b) Pasture (Field ID: 22)

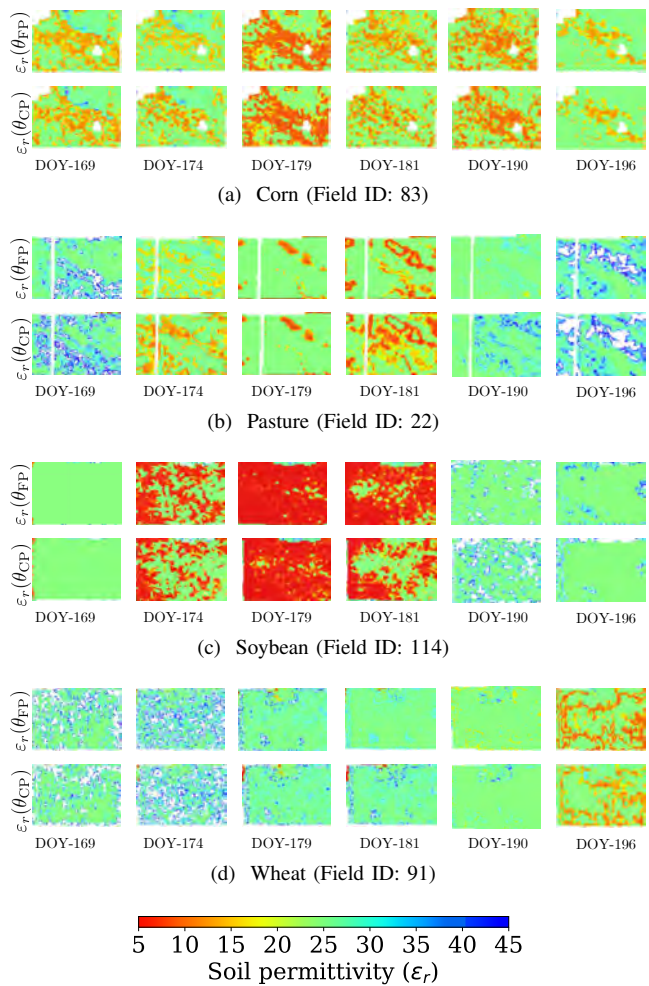(c) Soybean (Field ID: 114)

(d) Wheat (Field ID: 91)

Fig. 15. Temporal variation of soil permittivity at field scale for various crops. The top and bottom rows in each sub-figure correspond to soil permittivity derived from FP (θ_{FP}) and CP (θ_{CP}) SAR data, respectively.

V. CONCLUSIONS

This study proposes a unified method to estimate soil permittivity over croplands with vegetation cover using full polarimetric (FP) and compact polarimetric (CP) SAR data. The proposed method utilizes the recently proposed scattering-type parameter derived from the X-Bragg model. For FP SAR mode, the scattering type-parameter, θ_{FP} is obtained from the Eigen-decomposed polarimetric 3×3 coherency matrix $\mathbf{T}$, whereas for CP SAR mode, the scattering type-parameter, θ_{CP} is obtained from the Eigen-decomposed polarimetric 2×2 covariance matrix $\mathbf{C}$. The robustness of the proposed method resides in its generalized formulation for both the modalities: FP and CP.

The full and simulated compact polarimetric SAR data acquired by the airborne L-band Uninhabited Aerial Vehicle Synthetic Aperture Radar (UAVSAR) during the SMAPVEX12-MB campaign over the Carman test site in Canada are utilized for this study. We evaluated the performance of the proposed technique to estimate soil permittivity over four crops: corn, pasture, soybean, and wheat, for their major phenology stages.

A theoretical investigation suggests that the surface rough-

TABLE IV
SUMMARY OF PERMITTIVITY VALUES FROM FIELD-SCALE TEMPORAL ANALYSIS FOR ALL FOUR CROPS. EACH PERMITTIVITY VALUE INDICATES
MEAN±STANDARD DEVIATION. IN-SITU MEASUREMENTS ARE POINT OBSERVATION (16 SAMPLING POINTS FOR EACH FIELD), WHEREAS ESTIMATES ARE
OVER AN ENTIRE FIELD.

DOY	Corn (FID:83)			Pasture (FID:22)			Soybean (FID:114)			Wheat (FID:91)		
	In-situ ε_r	$\varepsilon_r(\theta_{FP})$	$\varepsilon_r(\theta_{CP})$	In-situ ε_r	$\varepsilon_r(\theta_{FP})$	$\varepsilon_r(\theta_{CP})$	In-situ ε_r	$\varepsilon_r(\theta_{FP})$	$\varepsilon_r(\theta_{CP})$	In-situ ε_r	$\varepsilon_r(\theta_{FP})$	$\varepsilon_r(\theta_{CP})$
169	15.19 ± 5.50	16.2 ± 3.24	17.12 ± 5.63	21.56 ± 11.29	22.34 ± 6.53	23.22 ± 8.23	–	23.23 ± 2.07	24.98 ± 3.28	12.82 ± 1.92	14.45 ± 3.70	15.60 ± 4.03
174	10.86 ± 4.48	12.23 ± 2.28	13.01 ± 3.83	23.39 ± 12.80	20.23 ± 3.72	22.56 ± 10.20	21.90 ± 6.09	16.54 ± 5.45	18.71 ± 7.73	12.59 ± 2.38	15.87 ± 5.20	17.02 ± 5.77
179	7.88 ± 3.20	8.21 ± 4.32	9.52 ± 4.56	20.85 ± 12.83	24.28 ± 11.69	25.67 ± 13.34	12.27 ± 3.30	6.27 ± 3.48	6.81 ± 4.32	6.78 ± 1.34	11.78 ± 3.90	13.14 ± 4.46
181	6.92 ± 2.68	9.72 ± 3.21	10.32 ± 4.35	17.16 ± 13.62	18.72 ± 10.23	19.47 ± 12.48	9.21 ± 2.41	10.76 ± 3.38	13.62 ± 5.40	–	12.88 ± 2.06	13.90 ± 4.91
190	16.39 ± 4.73	8.52 ± 2.31	9.37 ± 6.46	15.48 ± 11.88	21.46 ± 6.43	23.33 ± 8.56	13.80 ± 3.03	21.23 ± 4.38	24.66 ± 5.31	9.79 ± 1.82	11.44 ± 4.03	11.86 ± 5.38
196	–	19.21 ± 2.43	21.43 ± 5.23	–	24.55 ± 10.67	26.01 ± 13.98	–	19.80 ± 4.01	21.34 ± 5.11	–	8.82 ± 6.33	9.26 ± 7.81

ness less affects the proposed approach using θ compared to that of $\overline{\alpha}$ in the case of FP and χ in the case of CP. Therefore, the proposed method performs better than the existing methods in the presence of surface roughness.

The estimated permittivity using θ provided a good agreement with the in-situ measurements with a Root Mean Square Error ranging from 2.2 to 4.69 for FP and 3.28 to 5.45 for CP SAR data along with an $r \geq 0.62$. A comparative analysis with the existing scattering-type parameter $\overline{\alpha}$ proposed by Cloude and the ellipticity parameter χ apparently indicated better performance of the proposed approach by an average 12.4 % and 15.6 % RMSE for FP and CP SAR data respectively. However, due to the limitations of the X-Bragg model, we observed an increase in the error while estimating higher permittivity and advanced phenology stages. A similar increase in error was also reported in several previous studies. This error is more pronounced in estimates obtained from $\overline{\alpha}$ and χ compared to that of θ_{FP} and θ_{CP} respectively.

Nevertheless, these results provide new insight into using PolSAR data to retrieve soil permittivity for vegetated soils, an essential recommendation for the current operational mission like RADARSAT Constellation Mission (RCM) and future missions like NASA-ISRO SAR mission (NISAR), Biomass and Radar Observing System for Europe-L-band (ROSE-L).

APPENDIX

A. $\overline{\alpha}$ for Full-pol X-Bragg model:

$$\overline{\alpha}_{XB} = \frac{\lambda_{1_{XB}}\alpha_{1_{XB}} + \lambda_{2_{XB}}\alpha_{2_{XB}} + \lambda_{3_{XB}}\alpha_{3_{XB}}}{\lambda_{1_{XB}} + \lambda_{2_{XB}} + \lambda_{3_{XB}}}$$

where,

$$\lambda_{1_{XB}} = -0.5\beta^2\left(1 - \mathrm{sinc}\,(4\psi)\right) \tag{27}$$

$$\lambda_{2_{XB}} = 0.25\beta^2\left(\mathrm{sinc}\,(4\psi) + 1\right) + 0.5 + \frac{1}{2}$$
$$\left\{-\beta^2\left(-4\,\mathrm{sinc}^2\,(2\psi) + 2\,\mathrm{sinc}\,(4\psi) + 2\right)\right.$$
$$\left. + \left(0.5\beta^2\left(\mathrm{sinc}\,(4\psi) + 1\right) + 1\right)^2\right\}^{1/2} \tag{28}$$

$$\lambda_{3_{XB}} = 0.25\beta^2\left(\mathrm{sinc}\,(4\psi) + 1\right) + 0.5 - \frac{1}{2}$$
$$\left\{-\beta^2\left(-4\,\mathrm{sinc}^2\,(2\psi) + 2\,\mathrm{sinc}\,(4\psi) + 2\right)\right.$$
$$\left. + \left(0.5\beta^2\left(\mathrm{sinc}\,(4\psi) + 1\right) + 1\right)^2\right\}^{1/2} \tag{29}$$

$$\alpha_{1_{XB}} = \frac{\pi}{2} \tag{30}$$

$$\alpha_{2_{XB}} = \cos^{-1}\left(\left\{(\beta^2\,\mathrm{sinc}^2\,(2\psi))\left[0.25\beta^2\,\mathrm{sinc}\,(4\psi)\right.\right.\right.$$
$$+ 0.25\beta^2 - (0.0625\beta^4\,\mathrm{sinc}^2\,(4\psi)$$
$$+ 0.125\beta^4\,\mathrm{sinc}\,(4\psi) + 0.0625\beta^4$$
$$+ \beta^2\,\mathrm{sinc}^2\,(2\psi) - 0.25\beta^2\,\mathrm{sinc}\,(4\psi)$$
$$\left.\left.\left. - 0.25\beta^2 + 0.25)^{0.5} - 0.5\right]^{-2}\right\}^{1/2}\right) \tag{31}$$

$$\alpha_{3_{XB}} = \cos^{-1}\left(\left\{\beta^2\,\mathrm{sinc}^2\,(2\psi)\left[0.25\beta^2\,\mathrm{sinc}\,(4\psi)\right.\right.\right.$$
$$+ 0.25\beta^2 + (0.0625\beta^4\,\mathrm{sinc}^2\,(4\psi)$$
$$+ 0.125\beta^4\,\mathrm{sinc}\,(4\psi) + 0.0625\beta^4$$
$$+ \beta^2\,\mathrm{sinc}^2\,(2\psi) - 0.25\beta^2\,\mathrm{sinc}\,(4\psi)$$
$$\left.\left.\left. - 0.25\beta^2 + 0.25)^{0.5} - 0.5\right]^{-2}\right\}^{1/2}\right) \tag{32}$$

ACKNOWLEDGMENT

REFERENCES

[1] C. Champagne, A. Berg, H. McNairn, G. Drewitt, and T. Huffman, "Evaluation of soil moisture extremes for agricultural productivity in the Canadian prairies," *Agricultural and forest meteorology*, vol. 165, pp. 1–11, 2012.

[2] L. Karthikeyan, I. Chawla, and A. K. Mishra, "A review of remote sensing applications in agriculture for food security: Crop growth and yield, irrigation, and crop losses," *Journal of Hydrology*, vol. 586, p. 124905, 2020.

[3] K. Scipal, M. Drusch, and W. Wagner, "Assimilation of a ERS scatterometer derived soil moisture index in the ECMWF numerical weather prediction system," *Advances in water resources*, vol. 31, no. 8, pp. 1101–1112, 2008.

[4] N. Wanders, D. Karssenberg, A. De Roo, S. De Jong, and M. Bierkens, "The suitability of remotely sensed soil moisture for improving operational flood forecasting," *Hydrology and Earth System Sciences*, vol. 18, no. 6, pp. 2343–2357, 2014.

[5] Y. Oh, K. Sarabandi, and F. T. Ulaby, "An empirical model and an inversion technique for radar scattering from bare soil surfaces," *IEEE Trans. Geosci. Remote Sens.*, vol. 30, no. 2, pp. 370–381, March 1992.

[6] P. C. Dubois, J. Van Zyl, and T. Engman, "Measuring soil moisture with imaging radars," *IEEE transactions on geoscience and remote sensing*, vol. 33, no. 4, pp. 915–926, 1995.

[7] M. Borgeaud and J. Noll, "Analysis of theoretical surface scattering models for polarimetric microwave remote sensing of bare soils," *International journal of remote sensing*, vol. 15, no. 14, pp. 2931–2942, 1994.

[8] F. Mattia, T. Le Toan, J.-C. Souyris, C. De Carolis, N. Floury, F. Posa, and N. Pasquariello, "The effect of surface roughness on multifrequency polarimetric SAR data," *IEEE Transactions on Geoscience and Remote Sensing*, vol. 35, no. 4, pp. 954–966, 1997.

[9] I. Hajnsek, T. Jagdhuber, H. Schon, and K. P. Papathanassiou, "Potential of estimating soil moisture under vegetation cover by means of PolSAR," *IEEE Transactions on Geoscience and Remote Sensing*, vol. 47, no. 2, pp. 442–454, 2009.

[10] S. O. Rice, "Reflection of electromagnetic waves from slightly rough surfaces," *Communications on pure and applied mathematics*, vol. 4, no. 2-3, pp. 351–378, 1951.

[11] S. Cloude, K. Papathanassiou, and I. Hajnsek, "An Eigenvector Method for the Extraction of Surface Parameters in Polarmetric SAR," in *SAR workshop: CEOS Committee on Earth Observation Satellites*, vol. 450, 2000, p. 693.

[12] S. R. Cloude and D. Corr, "A new parameter for soil moisture estimation," in *IEEE International Geoscience and Remote Sensing Symposium*, vol. 1. IEEE, 2002, pp. 641–643.

[13] H. Moseley and C. Darwin, "The Reflection of the X-Rays." *Nature*, vol. 90, no. 2257, pp. 594–594, 1913.

[14] I. Hajnsek, "Inversion of surface parameters using polarimetric SAR," *PhD Thesis*, 2001.

[15] T. Jagdhuber, I. Hajnsek, A. Bronstert, and K. P. Papathanassiou, "Soil moisture estimation under low vegetation cover using a multi-angular polarimetric decomposition," *IEEE Transactions on Geoscience and Remote Sensing*, vol. 51, no. 4, pp. 2201–2215, 2012.

[16] T. Jagdhuber, I. Hajnsek, and K. P. Papathanassiou, "An iterative generalized hybrid decomposition for soil moisture retrieval under vegetation cover using fully polarimetric SAR," *IEEE Journal of Selected Topics in Applied Earth Observations and Remote Sensing*, vol. 8, no. 8, pp. 3911–3922, 2014.

[17] H. Wang, R. Magagi, and K. Goita, "Comparison of different polarimetric decompositions for soil moisture retrieval over vegetation covered agricultural area," *Remote Sensing of Environment*, vol. 199, pp. 120–136, 2017.

[18] H. Shi, J. M. Lopez-Sanchez, J. Yang, P. Li, L. Zhao, and J. Zhao, "Contribution of Polarimetry and Multi-Incidence to Soil Moisture Estimation Over Agricultural Fields Based on Time Series of L-Band SAR Data," *IEEE Journal of Selected Topics in Applied Earth Observations and Remote Sensing*, vol. 14, pp. 300–313, 2020.

[19] H. Wang, R. Magagi, K. Goita, and T. Jagdhuber, "Refining a polarimetric decomposition of multi-angular UAVSAR time series for soil moisture retrieval over low and high vegetated agricultural fields," *IEEE Journal of Selected Topics in Applied Earth Observations and Remote Sensing*, vol. 12, no. 5, pp. 1431–1450, 2019.

[20] H. Shi, L. Zhao, J. Yang, J. M. Lopez-Sanchez, J. Zhao, W. Sun, L. Shi, and P. Li, "Soil moisture retrieval over agricultural fields from L-band multi-incidence and multitemporal PolSAR observations using polarimetric decomposition techniques," *Remote Sensing of Environment*, vol. 261, p. 112485, 2021.

[21] W. An, Y. Cui, and J. Yang, "Three-component model-based decomposition for polarimetric SAR data," *IEEE Transactions on Geoscience and Remote Sensing*, vol. 48, no. 6, pp. 2732–2739, 2010.

[22] N. Stacy and M. Preiss, "Compact polarimetric analysis of X-band SAR data," in *Proc. EUSAR*, vol. 6, 2006.

[23] R. K. Raney, "Hybrid-polarity SAR architecture," *IEEE Transactions on Geoscience and Remote Sensing*, vol. 45, no. 11, pp. 3397–3404, 2007.

[24] J.-C. Souyris, P. Imbo, R. Fjortoft, S. Mingot, and J.-S. Lee, "Compact polarimetry based on symmetry properties of geophysical media: The $\pi/4$ mode," *IEEE Transactions on Geoscience and Remote Sensing*, vol. 43, no. 3, pp. 634–646, 2005.

[25] M.-L. Truong-Loi, A. Freeman, P. C. Dubois-Fernandez, and E. Pottier, "Estimation of soil moisture and faraday rotation from bare surfaces using compact polarimetry," *IEEE Transactions on Geoscience and Remote Sensing*, vol. 47, no. 11, pp. 3608–3615, 2009.

[26] J. D. Ouellette, J. T. Johnson, S. Kim, J. J. van Zyl, M. Moghaddam, M. W. Spencer, L. Tsang, and D. Entekhabi, "A simulation study of compact polarimetry for radar retrieval of soil moisture," *IEEE Transactions on Geoscience and Remote Sensing*, vol. 52, no. 9, pp. 5966–5973, 2014.

[27] E. Santi, M. Dabboor, S. Pettinato, and S. Paloscia, "Combining machine learning and compact polarimetry for estimating soil moisture from C-band SAR data," *Remote Sensing*, vol. 11, no. 20, p. 2451, 2019.

[28] A. Merzouki, H. McNairn, J. Powers, and M. Friesen, "Synthetic aperture radar (SAR) compact polarimetry for soil moisture retrieval," *Remote Sensing*, vol. 11, no. 19, p. 2227, 2019.

[29] G. G. Ponnurangam, T. Jagdhuber, I. Hajnsek, and Y. Rao, "Soil moisture estimation using hybrid polarimetric SAR data of RISAT-1," *IEEE Transactions on Geoscience and Remote Sensing*, vol. 54, no. 4, pp. 2033–2049, 2015.

[30] S. Dey, A. Bhattacharya, D. Ratha, D. Mandal, and A. C. Frery, "Target characterization and scattering power decomposition for full and compact polarimetric SAR data," *IEEE Transactions on Geoscience and Remote Sensing*, vol. 59, no. 5, pp. 3981–3998, 2020.

[31] S. Dey, A. Bhattacharya, A. C. Frery, C. Lopez-Martinez, and Y. S. Rao, "A model-free four component scattering power decomposition for polarimetric SAR data," *IEEE Journal of Selected Topics in Applied Earth Observations and Remote Sensing*, vol. 14, pp. 3887–3902, 2021.

[32] A. Freeman and S. L. Durden, "A three-component scattering model for polarimetric SAR data," *IEEE transactions on geoscience and remote sensing*, vol. 36, no. 3, pp. 963–973, 1998.

[33] Y. Cui, Y. Yamaguchi, J. Yang, H. Kobayashi, S.-E. Park, and G. Singh, "On complete model-based decomposition of polarimetric SAR coherency matrix data," *IEEE transactions on geoscience and remote sensing*, vol. 52, no. 4, pp. 1991–2001, 2013.

[34] J. J. Van Zyl, M. Arii, and Y. Kim, "Model-based decomposition of polarimetric SAR covariance matrices constrained for nonnegative eigenvalues," *IEEE Transactions on Geoscience and Remote Sensing*, vol. 49, no. 9, pp. 3452–3459, 2011.

[35] N. Bhogapurapu, S. Dey, A. Bhattacharya, C. López-Martínez, I. Hajnsek, and Y. Rao, "Soil Permittivity Estimation over Croplands Using PolSAR Data," in *IGARSS 2022-2022 IEEE International Geoscience and Remote Sensing Symposium*. IEEE, 2022, pp. 8000–8003.

[36] I. Hajnsek, E. Pottier, and S. R. Cloude, "Inversion of surface parameters from polarimetric SAR," *IEEE Transactions on Geoscience and Remote Sensing*, vol. 41, no. 4, pp. 727–744, 2003.

[37] N. Bhogapurapu, S. Dey, D. Mandal, A. Bhattacharya, L. Karthikeyan, H. McNairn, and Y. Rao, "Soil moisture retrieval over croplands using dual-pol L-band GRD SAR data," *Remote Sensing of Environment*, vol. 271, p. 112900, 2022.

[38] R. Sabry and P. W. Vachon, "A unified framework for general compact and quad polarimetric SAR data and imagery analysis," *IEEE Transactions on Geoscience and Remote Sensing*, vol. 52, no. 1, pp. 582–602, 2013.

[39] N. Bhogapurapu, S. Dey, D. Mandal, A. Bhattacharya, and Y. Rao, "PolSAR tools: A QGIS plugin for generating SAR descriptors," *Journal of Open Source Software*, vol. 6, no. 60, p. 2970, 2021.

[40] H. McNairn, T. J. Jackson, G. Wiseman, S. Belair, A. Berg, P. Bullock, A. Colliander, M. H. Cosh, S.-B. Kim, R. Magagi *et al.*, "The soil moisture active passive validation experiment 2012 (SMAPVEX12): Prelaunch calibration and validation of the SMAP soil moisture algorithms," *IEEE Transactions on Geoscience and Remote Sensing*, vol. 53, no. 5, pp. 2784–2801, 2015.

[41] S. Dey, A. Bhattacharya, D. Ratha, D. Mandal, H. McNairn, J. M. Lopez-Sanchez, and Y. S. Rao, "Novel clustering schemes for full and compact polarimetric SAR data: An application for rice phenology characterization," *ISPRS Journal of Photogrammetry and Remote Sensing*, vol. 169, pp. 135–151, 2020.

[42] M. B., Agriculture, "Agriculture Province of Manitoba," 2012. [Online]. Available: https://www.gov.mb.ca/agriculture/crops/seasonal-reports/crop-report-archive/index.html

[43] N. Bhogapurapu, S. Dey, A. Bhattacharya, D. Mandal, J. M. Lopez-Sanchez, H. McNairn, C. López-Martínez, and Y. S. Rao, "Dual-polarimetric descriptors from Sentinel-1 GRD SAR data for crop growth assessment," *ISPRS Journal of Photogrammetry and Remote Sensing*, vol. 178, pp. 20–35, 2021.

[44] N. Bhogapurapu, S. Dey, S. Homayouni, A. Bhattacharya, and Y. Rao, "Field-scale soil moisture estimation using sentinel-1 GRD SAR data," *Advances in Space Research*, 2022.

Narayanarao Bhogapurapu (S'19) received the B.E degree in Civil Engineering from Andhra University, India. He received the M. Tech degree in Remote sensing and GIS, Department of Civil Engineering, National Institute of Technology Warangal, India. He is currently pursuing a Ph.D. degree at the Microwave Remote Sensing Lab, Centre of Studies in Resources Engineering (CSRE), Indian Institute of Technology Bombay, India. His current research interests are soil moisture estimation, crop growth, and forest ecosystem monitoring using Polarimetric and Interferometric Synthetic Aperture Radar data. For this current work, he has been awarded the 2022 IEEE GRSS Mikio Takagi Student Prize at IGARSS 2022.

Subhadip Dey (S'17) received the B.Tech degree in Agricultural Engineering from Bidhan Chandra Krishi Viswavidyalaya, India. He received the M.Tech. degree in Aquacultural Engineering, Department of Agricultural and Food Engineering, Indian Institute of Technology Kharagpur, India, and Ph.D. degree from the Centre for Studies in Resources Engineering, Indian Institute of Technology Bombay. Dr. Dey was awarded with the DLR-DAAD postdoctoral fellowship to conduct his research at the German Aerospace Center, Oberpfaffenhofen, Germany. Currently, he is associated with the Department of Agricultural and Food Engineering, Indian Institute of Technology Kharagpur, India, as an Assistant Professor. His current research interests are aquacultural monitoring, advanced aquacultural techniques, precision agriculture, land cover classification, and agricultural crop mapping and monitoring using Synthetic Aperture Radar and optical sensors data.

Avik Bhattacharya (M'08–SM'16) received the integrated M.Sc. degree in Mathematics from the Indian Institute of Technology, Kharagpur, India, in 2000 and the Ph.D. degree in remote sensing image processing and analysis from Télécom ParisTech, Paris, France, and the Ariana Research Group, Institut National de Recherche en Informatique et en Automatique (INRIA), Sophia Antipolis, Nice, France, in 2007. He is currently an Associate Professor at the Centre of Studies in Resources Engineering, Indian Institute of Technology Bombay (CSRE, IITB), Mumbai, India. Before joining IITB, he was a Canadian Government Research Fellow at the Canadian Centre for Remote Sensing (CCRS) in Ottawa, ON, Canada. He received the Natural Sciences and Engineering Research Council of Canada visiting scientist fellowship at the Canadian national laboratories, from 2008 to 2011. His current research interests include SAR polarimetry, statistical analysis of polarimetric SAR images, applications of Radar Remote Sensing in Agriculture, Cryosphere, Urban and Planetary studies. Dr. Bhattacharya is the Editor-in-Chief of IEEE GEOSCIENCE AND REMOTE SENSING LETTERS (GRSL). He was an Associate Editor of IEEE GRSL. He has been the Guest Editor of the special issue on Applied Earth Observations and Remote Sensing in India in IEEE JOURNAL OF SELECTED TOPICS IN APPLIED EARTH OBSERVATIONS AND REMOTE SENSING (J-STARS), 2017. He was one of the guest editors of the special stream on Advanced Statistical Techniques in SAR Image Processing and Analysis in IEEE GEOSCIENCE AND REMOTE SENSING LETTERS, 2018. He is the Founding Chairperson of the IEEE Geoscience and Remote Sensing Society (GRSS) Chapter of the Bombay Section. He is currently leading the Microwave Remote Sensing Lab (www.mrslab.in) at CSRE, IITB.

Carlos López-Martínez (S'97-M'04-SM'11) received the MSc degree in Electrical Engineering and the PhD degree from the Universitat Politècnica de Catalunya UPC, Barcelona, Spain, in 1999 and 2003, respectively, as well as the Postgraduate Diploma in Data Science and Big Data from the Universitat de Barcelona UB, Barcelona, Spain in 2021. Dr. López-Martínez is Associate Professor in the area of remote sensing and microwave technology in the Universitat Politècnica de Catalunya, Barcelona, Spain. He has a large professional international experience at DLR (Germany), at the University of Rennes 1 (France), and as a group leader of the Remote Sensing and Natural Resources Modelling team in the Luxembourg Institute of Science and Technology (Luxembourg). His research interests include Synthetic Aperture Radar (SAR) theory, statistics and applications, multidimensional SAR, radar polarimetry, physical parameter inversion, advanced digital signal processing, estimation theory, and harmonic analysis. Dr. López-Martínez has authored more than 200 articles in journals, books, and conference proceedings, and received the EUSAR 2002 Conference Student Prize Paper Award, co-authored the paper awarded with the EUSAR 2012 Conference First Place Student Paper Award, and received the IEEE-GRSS 2013 GOLD Early Career Award. Dr. López-Martínez has broad academic teaching experience from bachelor, master, and PhD levels to advanced technical tutorials presented at international conferences and space and research institutions worldwide. He is an associate editor of the IEEE-JSTARS journal and the MDPI Remote Sensing, acting also as invited guest editor for several special issues. He has collaborated in the Spanish PAZ and the ESA's SAOCOM-CS missions, in the proposal of the Parsifal mission and he is member of the ESA's Sentinel ROSE-L Mission Advisory Group. He was appointed vice-president of the IEEE-GRSS Spanish chapter, and in 2016 he became its secretary and treasurer. From 2011 Dr. López-Martínez collaborates with the IEEE-GRSS Globalization initiative in Latin America, contributing to the creation of the IEEE-GRSS Chilean chapter and the organization of the 2020 LAGIRSS conference, being appointed as Latin America liaison in 2019. He is also co-chair of the Tutorial Technical Committee of the Indian 2020 and 2021 InGARSS conferences.

Irena Hajnsek (F'14) received the Dipl. degree (Hons.) in fluvial river systems from the Free University of Berlin, Berlin, Germany, in 1996, and the Dr. rer. nat. degree (Hons.) in model-based estimation of soil moisture from fully polarimetric synthetic aperture radar from the Friedrich Schiller University of Jena, Jena, Germany, in 2001.,Since November 2009, she has been a Professor of Earth observation with the Swiss Federal Institute of Technology (ETH) Zürich, Institute of Environmental Engineering, and at the same time Head of the Polarimetric SAR Interferometry research group, Microwaves and Radar Institute, German Aerospace Center, Weßling, Germany. Since 2010, she has been the Science Coordinator of the German Satellite Mission TanDEM-X and proposed satellite mission Tandem-L. Her research interests include electromagnetic propagation and scattering theory, radar polarimetry, SAR and interferometric SAR data processing techniques, and environmental parameter modeling and estimation.,Dr. Hajnsek is currently a member of the European Space Agency Mission Advisory Group for the ROSE-L Mission. She was the Technical Program Co-Chair of the IEEE International Geoscience and Remote Sensing Symposium (IGARSS) 2012, Munich, Germany, and the IEEE IGARSS 2019, Yokohama, Japan. Since 2013, she has been a member of the IEEE Geoscience and Remote Sensing Society (GRSS) AdCom. From 2016 to 2020, she was the Vice President of the IEEE GRSS Technical Committee.

Y. S. Rao received the M.Sc. degree in physics from Andhra University, India, in 1982, and the Ph.D. degree in passive microwave remote sensing of soil moisture from the Indian Institute of Technology (IIT) Bombay, Mumbai, in 1992. He joined the Centre of Studies Resources Engineering, IIT Bombay, in 1985, as a Senior Research Assistant and, then became a Research Scientist in 1999. During 2005–2009, he was a Senior Research Scientist and, then Associate Professor from 2009 to 2014. He is currently continuing as a Professor. He worked in both passive and active microwave remote sensing for several applications viz. soil moisture, flood mapping, and land use/land cover. He has participated in several spaceborne campaigns for collecting synchronous ground-truth data and has experience in handling various datasets for several applications. His research interests include application of polarimetry for geo-physical parameter retrieval and SAR interferometry for DEM and displacement map generation.